Cellular Level Brain Imaging in Behaving Mammals: An Engineering Approach

Elizabeth J.O. Hamel,[1] Benjamin F. Grewe,[1] Jones G. Parker,[1,2] and Mark J. Schnitzer[1,3,*]
[1]CNC Program, Stanford University, Stanford, CA 94305, USA
[2]Pfizer Neuroscience Research Unit, Cambridge, MA 02139, USA
[3]Howard Hughes Medical Institute, Stanford University, Stanford, CA 94305, USA
*Correspondence: mschnitz@stanford.edu
http://dx.doi.org/10.1016/j.neuron.2015.03.055

Fluorescence imaging offers expanding capabilities for recording neural dynamics in behaving mammals, including the means to monitor hundreds of cells targeted by genetic type or connectivity, track cells over weeks, densely sample neurons within local microcircuits, study cells too inactive to isolate in extracellular electrical recordings, and visualize activity in dendrites, axons, or dendritic spines. We discuss recent progress and future directions for imaging in behaving mammals from a systems engineering perspective, which seeks holistic consideration of fluorescent indicators, optical instrumentation, and computational analyses. Today, genetically encoded indicators of neural Ca^{2+} dynamics are widely used, and those of trans-membrane voltage are rapidly improving. Two complementary imaging paradigms involve conventional microscopes for studying head-restrained animals and head-mounted miniature microscopes for imaging in freely behaving animals. Overall, the field has attained sufficient sophistication that increased cooperation between those designing new indicators, light sources, microscopes, and computational analyses would greatly benefit future progress.

Introduction

For decades, the main technique for monitoring the dynamics of individual neurons in awake behaving mammals has been extracellular electrophysiological recording. Such recordings have yielded important and diverse advances in our knowledge of brain function. Heralded discoveries include those that related single-cell response properties to perceptual decisions and short-term memory, identified neurons with spiking patterns conveying spatial information about an animal's environment, and revealed neural computations underlying coordinate transformations crucial for directed body movements (Batista et al., 1999; Funahashi et al., 1989; Fuster and Alexander, 1971; Hafting et al., 2005; Newsome et al., 1989; O'Keefe and Dostrovsky, 1971). Today, although extracellular recording methods still retain unique advantages, particularly regarding temporal resolution, notable limitations persist regarding the difficulties of achieving stable long-term recordings for days to weeks, targeting cells by genetic type or connectivity, identifying cells with temporally sparse activity, sampling cells densely and in large numbers (i.e., many hundreds to a thousand cells in behaving mammals), and recording from dendrites, dendritic spines, or axons.

Over the last decade, optical imaging methods have rapidly advanced and emerged as increasingly potent means for cellular level recordings in behaving animals. To date, optical imaging and extracellular recording techniques have nicely complemented each other, as the strengths of the former coincide well with the above-mentioned weaknesses of the latter. Conversely, cellular level imaging of neural activity generally provides poorer temporal resolution than electrophysiological recording due to the usual reliance on fluorescent reporters of neural Ca^{2+} dynamics. In the last few years, genetically encoded fluorescent reporters of membrane voltage dynamics have also made substantial progress. This past year brought the visualization of single dendritic action potentials in the live mammalian brain using genetically encoded voltage indicators. Nevertheless, substantial further improvement in these indicators remains vital (Gong et al., 2014).

In this Review, we discuss significant recent advances in cellular imaging in behaving animals and likely directions of upcoming progress. We consider the issues from the viewpoint of systems engineering, which strives to optimize the overall performance of a technological system by taking into account the combined effects of all constituent elements, rather than considering them individually in isolation. When applied to an optical system for imaging neural activity, this holistic view seeks to optimize imaging performance by taking into account all pertinent factors, including the properties of the instrumentation and the neural activity indicator, the photon statistics underlying the detection of neural dynamics, and even data analyses. Considerations of photon statistics are fundamental to any discussion of action potential detection fidelity and timing estimation but may be unfamiliar to many readers. Hence, we start with background material to introduce this critical topic. We then discuss recent advances in optical indicators of neural activity, the complementary strengths of optical brain imaging in head-restrained versus freely behaving animals, computational algorithms for processing large-scale neural activity data, and the future outlook for the field.

Photon Statistics Underlying Detection of Neural Activity

Researchers have long sought meaningful ways to compare imaging systems that take into account the multiple factors

influencing the capacity to monitor neural activity with a fluorescent indicator. These factors include properties of the neural activity indicator such as its sensitivity, dynamic range of signaling, kinetics, brightness, absorption and emission spectra, and labeling efficiency. The properties of the optical instrumentation are generally of equal importance and include its numerical apertures of illumination and photon collection, resolution and optical sectioning capabilities, illumination intensity at the specimen, quantum efficiency of photon detection, dominant noise sources in the photo-detection process, and frame or pixel acquisition rates. Prior efforts to benchmark optical tools for monitoring neural dynamics often focused on neural activity indicators and characterized these through heuristic figures-of-merit or the use of standardized experimental formats to evaluate multiple indicators in a controlled way (Hendel et al., 2008; Hires et al., 2008; Sjulson and Miesenböck, 2007). However, it is crucial to have a principled theoretical framework on which to base comparisons.

Signal detection and estimation theories are frameworks from engineering that provide suitable mathematical principles to ground discussions of spike detection fidelity and the accuracy of spike timing estimation (Marshall and Schnitzer, 2013; Sjulson and Miesenböck, 2007; Wilt et al., 2013). An initial use of signal detection theory to describe the optical detection of neural action potentials correctly emphasized the physical limits on spike detection due to the inherent stochasticity of photon emission, transmission, and photodetection but failed to account for the time-varying optical signals that occur in response to a neural spike (Sjulson and Miesenböck, 2007). By applying signal detection theory to a more thorough, time-dependent mathematical model of the signals from an activity indicator, a more recent treatment derived a metric for the fidelity of neural spike detection under ideal experimental conditions in which photon number fluctuations, often termed photon "shot noise," are the limiting noise source (Wilt et al., 2013). This metric, symbolized as d', describes the physical limits of action potential detection and the severity of the tradeoff between false-positive and false-negative spike detection (Figure 1). (Readers may be familiar with the use of Cohen's d in statistics to characterize an effect size. Here d' can be thought of as the Cohen's d describing the magnitude of the effect that one action potential has on the photon flux.) Signal detection theory also enables principled comparisons between different indicators and instrumentation, allows benchmarking of different algorithms for spike extraction against the physical limits, provides means to gauge the statistical confidence of each detected spike, and quantifies how different optical parameters impact spike detection fidelity.

To illustrate, let's consider evaluations of different neural activity indicators. Signal detection theory elucidates the tradeoffs between sensitivity, dynamic range, kinetics, and brightness. Without this mathematical approach, the tradeoffs between these factors are hard to disentangle. For example, within the widely used GCaMP6 family of Ca^{2+} indicators there exist variants with a range of kinetics (Chen et al., 2013c). The more sensitive variants exhibit slower decays in fluorescence intensity following the occurrence of an action potential. Using the values from Table S3 of Chen et al. (2013c), the slowest variant, GCaMP6s, has only a slightly greater fluorescence response to

a single spike from a visual cortical neuron than the fastest variant, GCaMP6f, but nevertheless offers twice the spike detection fidelity (d') when the two are compared under otherwise equal optical conditions. However, GCaMP6f allows more accurate spike timing (Chen et al., 2013c), as described by signal estimation theory (see below). More generally, when evaluating different indicators one seeks to understand and summarize the net effects of differences in multiple signaling parameters. For instance, among the Fast-GCaMP Ca^{2+} indicators (Sun et al., 2013), there are large variations in brightness, signaling kinetics, and dynamic range; signal detection theory quantitatively describes how all these parameters interact.

The principled derivation of d' also shows that spike detection fidelity depends on more than just the dynamic range of signaling in response to a neural spike. (The latter quantity is often denoted $\Delta F/F$, to indicate the fractional change in fluorescence intensity.) Hence, evaluations of different indicators, optical instrumentation, and data analyses must properly consider all the contributing factors, including the detected fluxes of signal and background photons, and the temporal waveform of the indicator's response to a neural spike. Crucially, data sets with widely different values of $\Delta F/F$ can yield equally effective spike detection, because $\Delta F/F$ does not account for the total number and time course of background and signal photons detected per optical transient. In general, joint increases in both the background and signal photon flux attained by raising the illumination intensity will increase d'. This intensity is usually capped by the need to avoid fluorescence photobleaching and phototoxicity, so it is important to compare d' values for realistic imaging conditions. Moreover, in experiments with behaving animals, due to the substantial non-stationary noise from effects such as brain motion and hemodynamics, one generally cannot attain the physical limit on optical spike detection as expressed by d' values calculated for photon shot noise-limited conditions. Nevertheless, having this limit remains useful for making quantitative comparisons between the ideal cases in different optical situations. Empirical estimations of d' from actual data are also useful in that they convey how much an optical study falls short of the best-case scenario.

As a practical example of these ideas, the use of one-photon epi-fluorescence and two-photon laser-scanning fluorescence imaging modalities to detect cerebellar Purkinje neurons' complex spikes in live mice has yielded approximately equal spike detection fidelities (Wilt et al., 2013). However, under identical labeling conditions with a synthetic Ca^{2+} indicator, the two-photon imaging data exhibited $\Delta F/F$ values of ~10%–30%, whereas the one-photon data had $\Delta F/F$ values of ~1%–2% (Flusberg et al., 2008; Ghosh et al., 2011; Mukamel et al., 2009; Ozden et al., 2008). These general observations are broadly applicable; the differences in $\Delta F/F$ values stem from the lack of optical sectioning in one-photon epi-fluorescence imaging and the resulting increase in background fluorescence that diminishes image and signaling contrast. Unlike two-photon microscopy, which selectively excites fluorescence at the focal plane, in one-photon epi-fluorescence microscopy the fluorescence arising from planes even hundreds of microns outside the focal plane manifests as a substantial out-of-focus background flux that reduces the signaling contrast. Nevertheless, image pixels
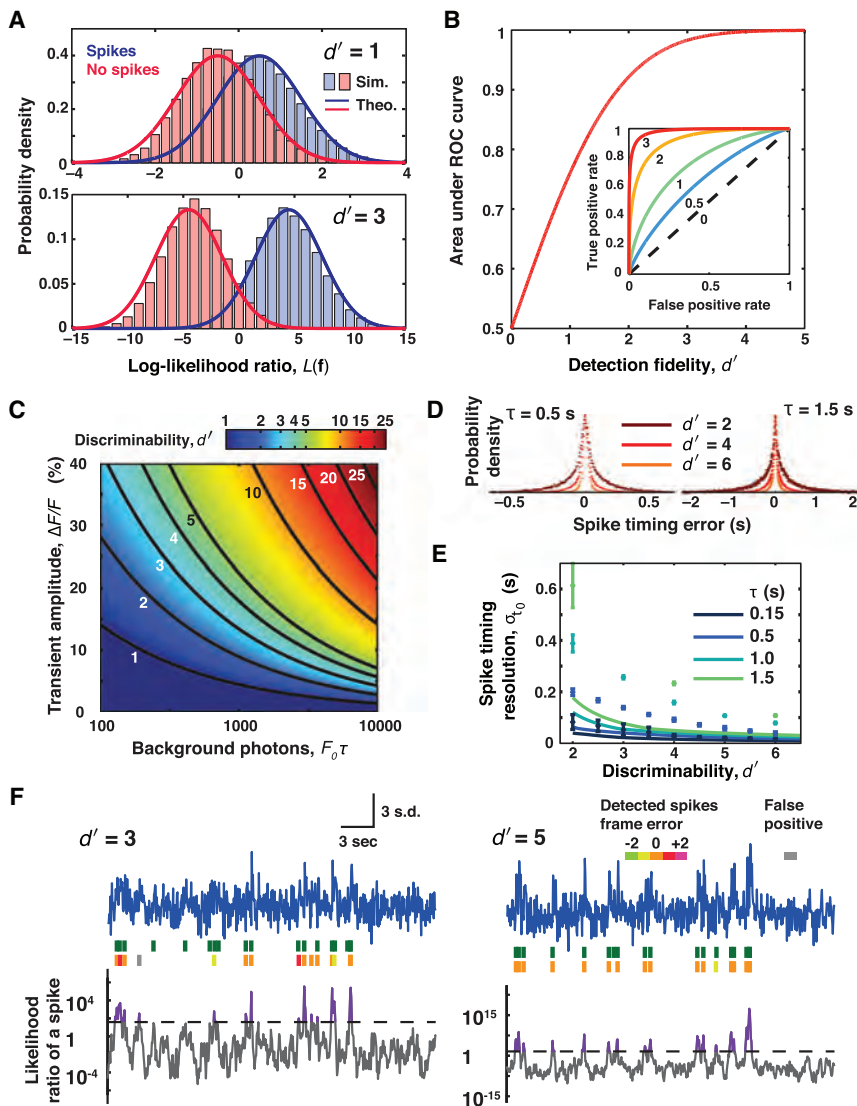
Figure 1. Signal Detection and Estimation Theories Quantify the Physical Limits of Spike Detection Fidelity and Spike Timing Estimation Accuracy in Optical Experiments

(A) Given a set of photodetector measurements, $\mathbf{f}$, the log-likelihood ratio $L(\mathbf{f})$ quantifies the relative odds that the measurements were of an action potential or not. In general, $\mathbf{f}$ can include data from multiple photodetectors or camera pixels and can extend over multiple time bins. Formally, $L(\mathbf{f})$ is a logarithm of a ratio of probabilities, greater than 0 if a neural spike is more likely to have occurred and less than 0 if it is more likely there was no spike. The decision of whether to classify $\mathbf{f}$ as representing a spike is enacted by setting a threshold value of $L(\mathbf{f})$; the exact value depends on the experiment's relative tolerances to false-positive versus false-negative errors. To analyze a full experiment one usually must make multiple classifications of this kind, across each successive time bin, to attain a digitized record of the spike train. Across the subset of all measurements that, in reality, represent the occurrence of a neural spike the mean value of $L(\mathbf{f})$ will be positive (blue data). Across all measurements in which no spike actually occurred, this mean value will be negative (red data). Comparison of the two probability distributions of $L(\mathbf{f})$, one for each of the two hypotheses, allows an assessment of how easy or challenging it is to distinguish the two cases. When the limiting noise source in the experiment is photon shot noise and the non-responsive, baseline photon flux is greater than the signal flux in response to a spike, the distribution of $L(\mathbf{f})$ for each of the two hypotheses is approximately Gaussian. The metric of spike detection fidelity, d', is the separation in the means of the two Gaussian distributions in units of their standard deviation and describes the degree to which the two hypotheses can be reliably distinguished. The greater the overlap area between the two distributions, the harder on average it is to distinguish if a spike occurred. Distributions of $L(\mathbf{f})$ for $d' = 1$ and $d' = 3$ are plotted using signal detection theory (solid lines) and from computer simulations of photon statistics (histograms).

(B) One formalizes the decision of whether a spike occurred or not by choosing a threshold value of $L(\mathbf{f})$ to serve as a decision cutoff that allows one to classify individual measurements, $\mathbf{f}$. *Inset*: Plotting the probability of successful spike detection against the probability of a false alarm for different values of the decision cutoff yields a curve known as the receiver operating characteristic (ROC) curve. Like d', the area under the ROC curve is a metric of spike detection fidelity that does not depend on the choice of decision threshold. Several ROC curves are plotted, indexed by their d' values. *Main panel*: The area under the ROC curve is plotted as a function of the d' value. Crucially, the area under the ROC curve quickly approaches unity as d' rises. This is because the overlap in the tails of the two Gaussian $L(\mathbf{f})$ distributions decreases faster than exponentially with increases in d' (panel A). A non-intuitive but important implication is that modest improvements in d', which has linear and polynomial relationships to the most common optical parameters, sharply reduce the spike detection error rate. Hence, incremental improvements to indicators, cameras, and other optical hardware can yield huge dividends toward successfully capturing neural activity.

(C) d' depends on the signal amplitude of the neural activity indicator's response to an action potential and on the mean number of background photons collected during the indicator's optical transient. When the Gaussian approximation is valid, and the fluorescence emissions comprise a stationary mean baseline flux, F_0, plus a modest signal transient that arises nearly instantaneously at each spike incidence and then decays exponentially with time constant τ, the expression for d' reduces to approximately $(\Delta F/F) \cdot \sqrt{(F_0 \tau/2)}$. This shows that indicators with prolonged optical signal transients improve spike detection, since analyses can make use of the signal photons that arrive over the transient's entire duration. At a constant value of $\Delta F/F$, signal detection improves with increasing background due to the concomitant increase in signal photons.

(D) Simulations of spike timing resolution. Using a brute-force maximum likelihood method for estimating the spike time, histograms of the spike timing error for two indicators with distinct signaling kinetics are shown. Note the different time scales on the two panels. For visual clarity, histograms are normalized to a common peak value. Simulations used 50 ms time bins.

(E) Plots of simulated spike timing resolution and the theoretically calculated Chapman-Robbins lower bound on spike timing estimation errors. The simulations (points) generally do not attain the Chapman-Robbins lower bound (lines), especially for situations with low SNR and slow temporal dynamics. The Chapman-Robbins lower bound should be considered a best-case for estimation variance.

(F) Simulated optical traces and detected spikes for $d' = 3$ and $d' = 5$. Blue traces: optical measurements shown in units of the standard deviation from the mean photon count. Green spikes: the true spike train. Orange spikes: correctly estimated spikes. Spikes in non-orange hues: spikes estimated with errors in frame timing. Gray spikes: false positives. Gray trace: $L(\mathbf{f})$ for a moving window of nine time bins. Dashed black line: spike detection threshold given equal costs for false positives and false negatives. Purple: threshold crossings. Spikes were detected using an iterative algorithm that assigned a spike to the instance of the log-likelihood ratio's maximum in each iteration. At low d', few spikes are detected with this choice of threshold.

All panels are adapted from Wilt et al. (2013).

in two-photon microscopy are generally sampled serially, and laser dwell times per pixel are typically ∼0.1–3 μs. By comparison, in one-photon epi-fluorescence microscopy entire image frames are usually taken in acquisition times of ∼10–100 ms. Thus, even though the one-photon video data might seem less impressive by eye due to the lower $\Delta F/F$ values, the detection of Ca^{2+} transients is usually based on many more photons than in two-photon imaging data sets. In many common situations (but certainly not all), the magnitudes of the two counteracting effects approximately offset each other under normal imaging conditions, yielding comparable values of d' for the two imaging modalities (Wilt et al., 2013). These considerations are germane to efforts to increase the number of cells that one can monitor per unit time. Imaging modalities based on serial laser-scanning strategies are subject to basic, photon-limited tradeoffs between the number of cells that can be sampled and the attainable time-resolution and d' values. Modalities in which many pixels are optically monitored in parallel might be more easily expanded to larger sets of cells without compromising d' values, provided that suitable optics and detection systems exist to sample broad fields of view.

Notwithstanding, a key strength of two-photon microscopy in this discussion is its optical sectioning and rejection of background fluorescence, which in turn prevents the diminution of the signaling dynamic range seen in one-photon microscopy. Signal detection and spatiotemporal resolution are distinct concepts in engineering and physics, but as in this example superior resolution generally aids signal detection. Nevertheless, it is well known that one can sometimes detect signals from sources that are not resolved, and there are multiple longstanding techniques in optical microscopy that do exactly that (Wilt et al., 2009). The distinction between resolution and detection will be familiar to those versed in biophysical imaging studies of single fluorescent molecules and associated methods of super-resolution microscopy (Wilt et al., 2009), which involve the detection of single fluorescent emitters. In both neural imaging and single-molecule studies, signals from structures that cannot be separately resolved may be distinguishable using statistical methods, even if they are sometimes concurrently active—provided their activity is sometimes asynchronous. The temporal asynchrony aids the disentanglement of signals that are inseparable by spatial resolution alone; however, the more neural sources that need to be computationally disentangled in this way and the greater their synchronous activation, the more challenging this task becomes. More broadly, attaining high-quality Ca^{2+} traces requires suitable algorithms for extracting individual cells' dynamics from the raw Ca^{2+} imaging data. This is especially so with one-photon fluorescence microscopy, which does not provide optical sectioning, since Ca^{2+} signals from out of focus neural elements will impact the image data. To prevent these contaminants from causing substantial artifacts or cross talk in the traces representing the dynamics of individual cells, it is generally important to use cell-sorting algorithms capable of cross talk removal (see Computational Image Analyses). Cross talk from neurons far outside the focal plane is not a concern with two-photon imaging, but signal contaminants can still arise from neuropil or at the boundaries between adjacent cells (Kerr et al., 2005; Mukamel et al., 2009). Given

the prominent role that optical detection of neural activity is likely to play in neuroscience research for the foreseeable future, an acquaintance with signal processing and signal detection theory will become increasingly useful (Figure 1).

An important result to emerge from a signal detection theoretic analysis of spike detection is that even though d' varies linearly, sub-linearly, or as a polynomial function of common optical parameters, incidence rates of false-positive or false-negative spike detection fall faster than exponentially with increases in d'. This has practical consequences, because it implies that modest improvements to indicators, cameras, and other optical hardware can yield major strides toward successfully capturing neural activity. Another key result from signal detection theory is that in the regime of low fluorescence background, spike detection can succeed well with even modest numbers of signal photons. An activity indicator with ultra-low levels of baseline emission can thus be highly effective, even if signal emission in response to neural activity is weak. This result may seem non-intuitive, since for many fluorescence reporters protein engineers seek to optimize brightness. However, much of the improved performance of GCaMP6 over its predecessors is due to diminished baseline fluorescence, rather than increased signal emission (Chen et al., 2013c). This theoretical result also illustrates the value of the systems engineering approach for indicator development and provides the mathematical basis for why the NIH BRAIN Initiative report calls for indicators with ultra-low background emissions (BRAIN Initiative, 2014).

Across a wide range of conditions, if the fluorescence emissions comprise a stationary mean baseline flux, F_0, plus a signal transient that arises nearly instantaneously at spike incidence and then decays exponentially with time constant τ, the theoretical expression for d' under photon shot noise-limited conditions is approximately $(\Delta F/F) \cdot \sqrt{(F_0 \tau/2)}$. The first factor implies that d' increases linearly with the signaling dynamic range, whereas the second factor implies that increases in brightness or extensions of the decay time that do not affect $\Delta F/F$ lead only to square root improvements in d'. This captures mathematically the notion that indicators with prolonged signal transients improve spike detection, since analyses can make use of the signal photons that arrive over the transient's entire duration (Figure 1C). More broadly, this expression for d' facilitates comparative evaluations and describes how changes in instrumentation that impact F_0, such as an increase in camera sensitivity or a decrease in the numerical aperture of photon collection, impact spike detection fidelity. One can also examine rise-time kinetics, and signal detection theory shows that spike detection fidelity generally declines with slowing of the optical transient's rise time.

In many experiments, researchers aim not only to detect spike incidences but also to estimate the times of their occurrences. As noted above, increasing the duration of the optical transient in response to a neural spike increases d', but it reduces the accuracy of spike timing estimation. The Chapman-Robbins (C-R) bound is a metric from signal estimation theory that provides a theoretical minimum for the variance in the estimation of spikes' occurrence times. Under photon shot noise-limited conditions, the C-R bound can imply an optimal timing estimation accuracy that is either smaller or greater than the time bin used to sample

the photon flux. This implies that "super-resolution" in the estimation of spike timing may be possible, such as by using prior knowledge of the signal's temporal waveform (Grewe et al., 2010). The C-R bound generally depends most strongly on d' and τ (Wilt et al., 2013) (Figures 1D and 1E). Unlike signal detection theory, which provides concrete prescriptions for classifying the occurrences of spikes, signal estimation theory does not guarantee the existence of an estimator that attains the C-R bound. Nonetheless, the C-R lower bound provides a best-case value of estimation variance and useful guidance regarding the optical parameters that influence spike timing accuracy in real experimental situations.

Together, the engineering frameworks discussed here provide valuable insights toward optimizing optical experiments. Notably, the formalism describes how modifications in instrumentation or data acquisition rates trade off with changes in indicator properties. In this sense, the analyses help meet the aims of the systems engineer, who seeks to consider all facets of an imaging system or experiment holistically.

Neural Activity Indicators

To date, imaging studies of cellular level neural activity in live mammals have nearly all relied on indicators of intracellular Ca^{2+} concentration, $[Ca^{2+}]$. (Notable exceptions include studies of vesicle, glutamate, or monoamine release [Kato et al., 2012; Marvin et al., 2013; Muller et al., 2014].) Initial Ca^{2+} imaging studies used small molecule Ca^{2+}-sensitive dyes, several of which are bright, are photostable, and report neural Ca^{2+} transients in the live brain via fluorescence transients of ~150 ms durations and $\Delta F/F$ values up to ~150%–200% in isolated labeled cells (Helmchen et al., 1999; Svoboda et al., 1999). The advent of methods for bulk loading Ca^{2+}-sensitive dye into many cells in the live brain opened the door to in vivo Ca^{2+} imaging studies of neuronal and astrocytic ensembles (Nimmerjahn et al., 2004; Stosiek et al., 2003). However, reliable targeting of a Ca^{2+}-sensitive dye to selected cells in the live mammalian brain is usually achieved by visually guided intracellular loading, such as by maneuvering a micropipette (Kitamura et al., 2008), which impedes the study of large populations of cells of a single genetic class. Emerging chemical genetic methods may combine bulk loading of an indicator dye with genetic specificity (Tian et al., 2012). An existing alternative is to use one fluorescence color channel for detecting Ca^{2+} signals across a broad population of indicator labeled cells and another color channel for identifying a subset of cells that express a fluorescent genetic marker (Kerlin et al., 2010; Nimmerjahn et al., 2004; Runyan et al., 2010).

The arrival of genetically encoded Ca^{2+} indicators with comparable signaling performances as those of synthetic Ca^{2+}-sensitive dyes has enabled fairly routine targeting of genetically defined cell populations in live mammals (Chen et al., 2013c; Ohkura et al., 2012; Tian et al., 2009). One does need genetic access to the cells of interest, but for many cell types suitable genetic tools exist. Notably, genetically encoded Ca^{2+} indicators can often be expressed stably over weeks, sometimes months; thus, unlike Ca^{2+}-sensitive dyes, genetically encoded indicators allow long-term imaging studies of neural dynamics in behaving animals through the use of chronic animal preparations (Ander-

mann et al., 2010; Chen et al., 2013c; Huber et al., 2012; Keck et al., 2013; Masamizu et al., 2014; Peters et al., 2014; Ziv et al., 2013). Time-lapse Ca^{2+} imaging studies have opened up to empirical study many questions about the long-term dynamics of ensemble neural codes—in hundreds of neurons per animal—that were previously unanswerable. A key part of the toolkit enabling these capabilities is the widely used GCaMP family of genetically encoded Ca^{2+} indicators.

GCaMP comprises a circularly permuted green fluorescent protein (GFP) into which a calmodulin Ca^{2+}-sensing domain with four Ca^{2+} ion-binding sites is inserted (Nakai et al., 2001). Binding of one or more Ca^{2+} ions to the calmodulin moiety modulates the protein's conformation and the environment surrounding the GFP fluorophore such that it increases its fluorescence intensity. Several rounds of protein engineering have markedly improved the GCaMP indicators' signaling capabilities (Chen et al., 2013c; Ohkura et al., 2012; Tian et al., 2009). An advanced variant, GCaMP6, is today widely used for in vivo cellular-level functional imaging, comes in distinct versions representing different tradeoffs between detection sensitivity and signaling kinetics, approaches single-spike detection sensitivity, and allows a spike timing resolution of ~10–250 ms depending on the experimental details and data analyses (Chen et al., 2013c). Ongoing work seeks to create Ca^{2+} indicators based on fluorophores with emission colors other than green (Akerboom et al., 2013; Inoue et al., 2015; Wu et al., 2013; Zhao et al., 2011). As recently demonstrated in live mice expressing red and green Ca^{2+} indicators in neocortical somatostatin interneurons and pyramidal cells, respectively, there are interesting possibilities for probing information processing in two or more distinct cell types simultaneously (Inoue et al., 2015). Red fluorescent Ca^{2+} indicators also offer the prospect of imaging more deeply into brain tissue, due to the reduction in light scattering at longer optical wavelengths.

Notwithstanding the utility of Ca^{2+} imaging, it does not provide an exact readout of membrane voltage dynamics. The time course of the $[Ca^{2+}]$ rise in response to an action potential is governed by biophysical processes, including Ca^{2+} buffering and voltage-dependent activation of Ca^{2+} channels, which are distinct from those setting the action potential's electrical waveform (Helmchen et al., 1996). The time-varying signals from a Ca^{2+} indicator also depend strongly on its Ca^{2+} handling properties, notably the kinetic rates and equilibrium constant for Ca^{2+} binding and unbinding (Sun et al., 2013). Thus, in addition to the inherent differences between membrane voltage and intracellular $[Ca^{2+}]$ dynamics, fluorescence signals from a Ca^{2+} indicator provide a temporally filtered version of the underlying $[Ca^{2+}]$ dynamics. There are also nonlinear aspects of the temporal filtering, such as due to Ca^{2+} binding saturation or cooperativity in the binding of multiple Ca^{2+} ions to an indicator molecule (Nakai et al., 2001; Tian et al., 2009).

For GCaMP6, simultaneous optical and electrical recordings in vitro have revealed that CA1 hippocampal pyramidal cells have an approximately linear relationship between the peak amplitude of a somatic Ca^{2+} transient and the underlying number of action potentials (Chen et al., 2013c). Other types of pyramidal cells likely also exhibit approximately linear relationships between these variables, but not necessarily with the same linear

function as for CA1 pyramidal cells. Inhibitory interneurons typically differ in their spiking patterns and Ca^{2+} signaling and buffering attributes from excitatory neurons, which usually makes it harder to assign spike numbers to interneurons' Ca^{2+} transients. Nevertheless, Ca^{2+} imaging can often reveal a general, time-dependent modulation of interneuron activity. For example, Ca^{2+} imaging studies of the response properties of visual cortical interneurons have tracked visually evoked rises in somatic fluorescence intensity, which approximated spike rate modulations, rather than discrete incidences of Ca^{2+} transients (Kerlin et al., 2010; Runyan et al., 2010). More broadly, interneurons or other cell classes with fast-spiking patterns challenge the capabilities of Ca^{2+} indicators, which cannot provide millisecond-scale timing or accurately follow the individual action potentials in a spike burst, due to the optical transients' prolonged decay times ($\sim$150 ms or more) and moderate rise times ($\sim$10 ms or more). If a Ca^{2+} indicator is sparsely expressed in isolated cells, one can detect the activation of individual dendrites, dendritic spines, or axons (Chen et al., 2013c; Glickfeld et al., 2013; Kaifosh et al., 2013; Lovett-Barron et al., 2014; Xu et al., 2012), but it is generally infeasible to monitor hyperpolarizations or other sub-threshold aspects of somatic voltage dynamics in vivo by using Ca^{2+} imaging.

Thus, the attraction of voltage indicators stems from the possibility of directly visualizing neural membrane voltage and tracking fast and sub-threshold dynamics that Ca^{2+} signals fail to convey. The challenge of developing high-performance voltage indicators results from: the brief durations of spike waveforms (as short as hundreds of microseconds in some neuron types), necessitating indicators with comparably rapid on-kinetics; the desire to follow individual spikes in a burst, precluding the use of prolonged signal decays to boost detection fidelity; the need to target the indicator to the cell membrane with high selectivity to sense the membrane potential and avoid non-specific background fluorescence; the more limited portion of the cell (the membrane, a two-dimensional structure) from which useful photonic signals arise, as compared to the cytoplasm in Ca^{2+} imaging; and the need for much higher d' values due to the far briefer time bins ($\sim$1 ms) typically used for imaging voltage versus Ca^{2+} dynamics. The last point follows from signal detection theory (Figure 1B). To illustrate, if the probability of correctly categorizing one time bin as containing a spike or not is 0.99, and the time bin is 100 ms, this implies that the mean rate of false-positive spike detection is on the order of 0.1 Hz. But if the time bin is 1 ms, the false-positive rate becomes $\sim$10 Hz, which is unacceptable and can swamp the true spiking patterns of many neurons.

Small-molecule voltage-sensitive fluorescent dyes have been in use for several decades. The best of these are bright and have fluorescence dynamic ranges of up to $\sim$20%–50% per 100 mV voltage change when excited near the red-edge of their absorption spectrum (Kuhn et al., 2008). However, they tend to be lipophilic, labeling cell membranes indiscriminately, and highly prone to photobleaching and phototoxic effects on cell health (Peterka et al., 2011). With bulk loading approaches it is also challenging to discriminate voltage signals arising from individual cells from those emanating from neighboring cells or neuropil. Targeted intracellular loading of dye into individual cells is

feasible (Antić and Zecević, 1995), but this approach is ill-suited for in vivo imaging of large ensembles of individual cells or for long-term imaging studies.

Genetically encoded voltage indicators can be readily targeted to chosen cell types and in principle should permit long-term imaging studies of voltage dynamics. In the last few years, protein voltage indicators have markedly improved in sensitivity, brightness, dynamic range, and signaling kinetics. One class of these indicators takes advantage of the conformational dynamics of a voltage-sensing domain (VSD) isolated from a voltage-sensitive phosphatase of the sea squirt *Ciona intestinalis.* Fusing this VSD to two bright fluorescent proteins that serve as fluorescence resonance energy transfer (FRET) pairs yielded bright voltage sensors (Akemann et al., 2012, 2010; Dimitrov et al., 2007; Tsutsui et al., 2008). These sensors exhibit $\sim$20–100 ms response times to voltage depolarizations and have recently allowed cell-type-specific imaging of population level voltage dynamics in awake animals (Carandini et al., 2015). However, their signaling dynamic range is limited ($\sim$1% response to action potentials in cultured cells) due to various combinations of weak voltage sensitivity and slow kinetics. The ArcLight voltage indicator is also based on the *Ciona intestinalis* VSD, but fused to a single fluorescent protein (Cao et al., 2013; Jin et al., 2012). ArcLight attains $\sim$12 ms response times and <3% signal changes in response to action potentials, but its decay kinetics limit its ability to resolve spikes separated by less than $\sim$50 ms. These attributes sufficed in live fruit flies to convey useful aspects of voltage dynamics in specific neurons with relatively slow voltage dynamics (Cao et al., 2013) but are generally insufficient to report fast spike trains.

Another class of voltage indicators uses bacteriorhodopsin family proteins as the voltage-sensitive element. During the proton pumping photocycle of these proteins such as Archaerhodopsin (Arch), which is well known in neuroscience for providing a means of optogenetic silencing (Chow et al., 2010), there are changes in optical absorbance that accompany proton translocation (Kralj et al., 2012; Lanyi, 2004). These proteins are also very weakly fluorescent (quantum yield $<10^{-3}$) (Kralj et al., 2012). Thus, changes in the proton-motive force, i.e., through changes in pH or trans-membrane voltage, modulate the absorbance and thus confer voltage sensitivity to the fluorescence intensity (Kralj et al., 2012; Kralj et al., 2011). Initial work identified a mutation that eliminated Arch's proton current but slowed the photocycle and sensor kinetics (Kralj et al., 2012). Other mutations sped the voltage-dependent kinetics and improved the dynamic range ($\sim$10%–50% $\Delta F/F$ for spikes in cultured neurons) while maintaining negligible photocurrent (Flytzanis et al., 2014; Gong et al., 2013; Hochbaum et al., 2014). The larger dynamic range and faster kinetics enabled spike detection in cultured neurons at d' levels several-fold greater than those of the initial Arch sensor (Gong et al., 2013; Hochbaum et al., 2014). However, in brain slices Arch's dim fluorescence necessitates intense illumination ($\sim$12 W/mm^2) that excites tissue auto-fluorescence and heats the specimen (Hochbaum et al., 2014). Toward enabling studies in behaving mammals, efforts to create brighter Arch variants are underway (Flytzanis et al., 2014; Hochbaum et al., 2014; McIsaac et al., 2014).
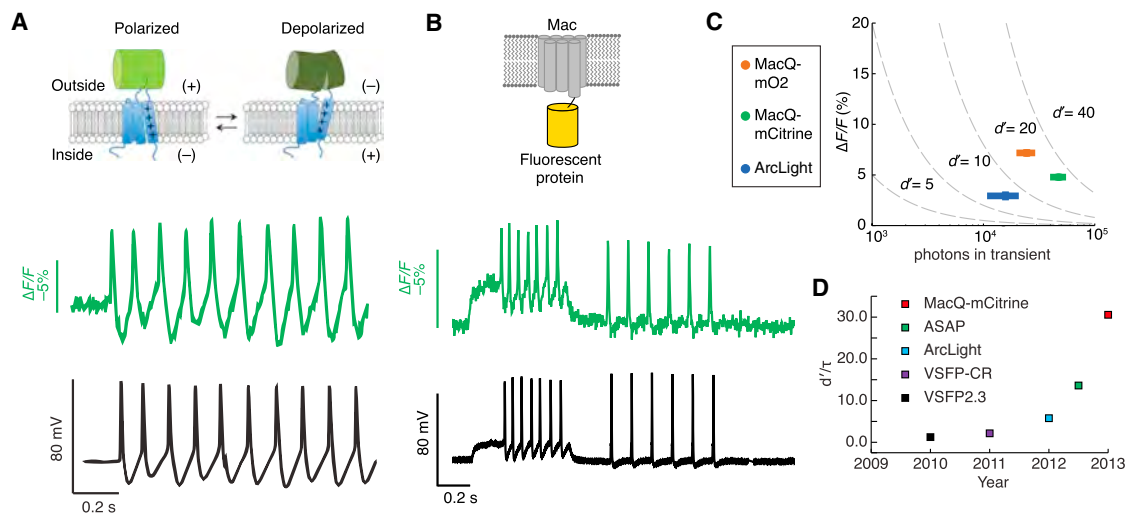
Figure 2. Recent Advances in Genetically Encoded Fluorescent Voltage Indicators
(A) *Upper*: Design of the ASAP1 voltage sensor. A circularly permuted green fluorescent protein is inserted within an extracellular loop of the VSD from a chicken voltage-sensitive phosphatase. Depolarization leads to decreased fluorescence. *Lower*: Simultaneously acquired optical (green) and electrophysiological (black) recordings from a cultured hippocampal neuron expressing ASAP1 and undergoing a spontaneous burst of action potentials.
(B) *Upper*: Design of a FRET-opsin voltage sensor. An *L. maculans* (Mac) rhodopsin is fused to a bright fluorescent protein. *Lower*: Simultaneously acquired optical (green) and electrophysiological recordings (black) from a cultured neuron expressing MacQ-mCitrine.
(C) For a set of measurements performed under standardized optical conditions, peak $\Delta F/F$ values are plotted against the total number of photons detected per spike. Dashed lines are iso-contours of the spike detection fidelity index d'.
(D) Genetically encoded voltage indicators have notably improved over the past several years. Whereas d' measures spike detection fidelity for temporally isolated spikes, d'/τ, where τ is the indicator's decay time-constant, captures the capabilities of sensors with faster off-times to detect spikes within fast spike trains.
(A) is adapted from St-Pierre et al. (2014). (B) and (C) are adapted from Gong et al. (2014). (D) is courtesy of Y. Gong.

Two new classes of genetically encoded voltage indicators with notably improved capabilities advance the field closer to tracking the membrane potentials of individual neurons optically in live mammals. The ASAP1 indicator consists of a circularly permuted green fluorescent protein inserted within an extracellular loop of the VSD from a chicken voltage-sensitive phosphatase, yielding a sensor that declines in fluorescence intensity with membrane depolarization (Figure 2A) (St-Pierre et al., 2014). This represents a distinct voltage-sensing mechanism from ArcLight, which has an intracellular fluorophore fused to the C terminus of the VSD. In comparison, FRET-opsin indicators combine the brightness of a genetically engineered fluorescent protein, which acts as a FRET donor, with the voltage-sensitive absorbance of a rhodopsin family protein, which acts as a FRET acceptor (Gong et al., 2014; Zou et al., 2014). This approach also yields declines in fluorescence with membrane depolarization. The FRET-opsin sensors MacQ-mOrange2 and MacQ-mCitrine employ the *L. maculans* (Mac) rhodopsin molecule, which in comparison to Arch has greater voltage sensitivity and a blue-shifted absorption spectrum that allows better spectral overlap with the emissions of bright fluorescent proteins (Figure 2B) (Gong et al., 2014).

ASAP1 and the Mac sensors have comparably fast kinetics, with ∼2–3 ms time constants for the fast on-component of the fluorescence response. They are also sufficiently bright to overcome tissue auto-fluorescence and successfully report single action potentials in live brain slices, at illumination intensities ∼500–1,000 times lower than those used for Arch (Gong et al.,

2014; Hochbaum et al., 2014; St-Pierre et al., 2014). For detection of neural spikes, the MacQ sensors outperform ArcLight by ∼2-fold in d' (Figures 2C and 2D). Reflecting the sharp decline in spike detection error rates with rises in d' (Figure 1B), this ∼2-fold increase should substantially improve voltage-imaging performance in challenging experiments. To illustrate, an improvement from $d' = 2$ to $d' = 4$ should theoretically decrease the spike detection error rate from ∼10^{-1} to ∼10^{-3} per time bin. In live mice, the rates and optical waveforms of cerebellar Purkinje neurons' dendritic voltage transients as seen via MacQ-mCitrine matched expectations based on electrophysiological recordings. However, the choice of Purkinje neurons for this demonstration was specifically motivated by these neurons' large dendritic trees and the prolonged duration of their dendritic spikes, factors that substantially eased the challenge of spike detection (Gong et al., 2014).

Overall, voltage indicators are nearing the performance levels needed to image single action potentials in the brains of behaving mammals, at least under sparse labeling conditions. To achieve this, calculations suggest that ∼2- to 4-fold further increases in d' values will be required, and even greater increases for imaging densely labeled cells. Along with further improvements to the indicators, advances in optical instrumentation will be crucial to bring voltage imaging to full fruition in behaving animals (see Outlook). The microscopes in common use today for Ca^{2+} imaging in behaving animals are typically incapable of the kilohertz imaging rates needed for the analogous voltage-imaging studies. To acquire voltage-imaging data
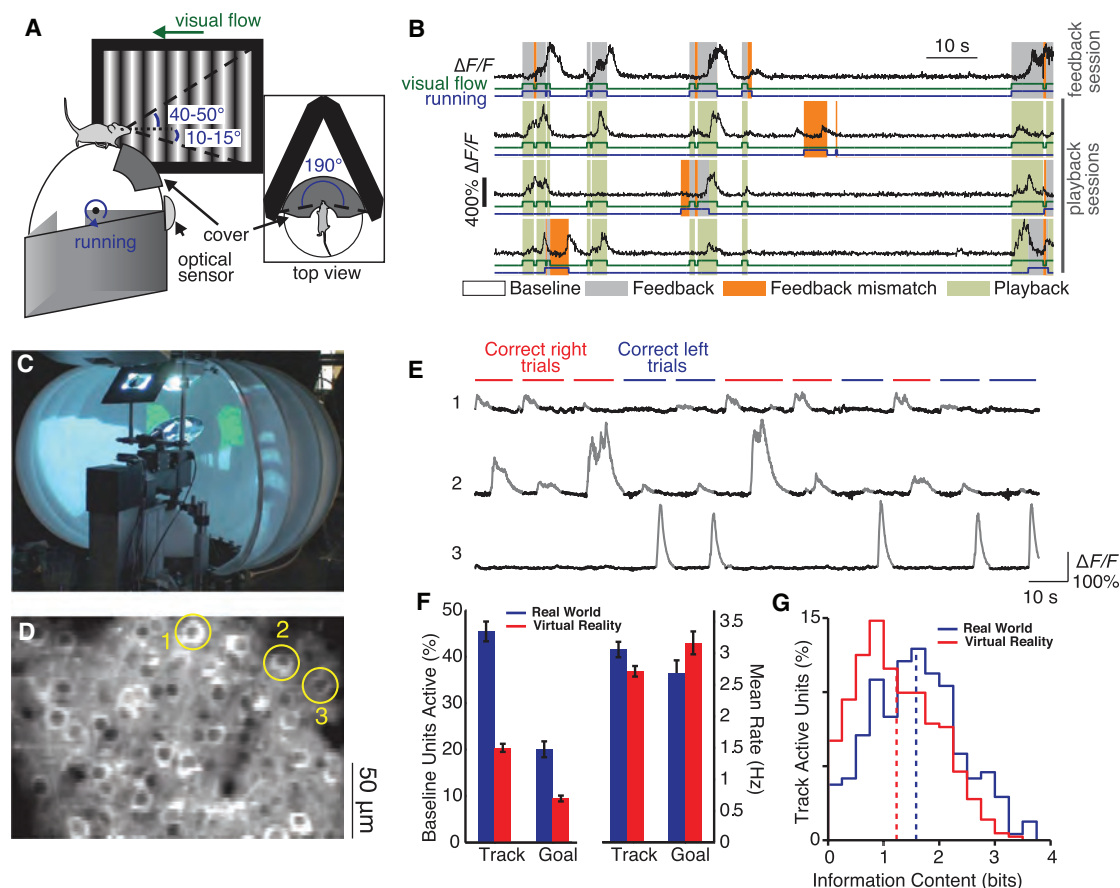
Figure 3. Head Fixation Allows Cellular Level Brain Imaging using Conventional Optics, while Constraining and Enhancing Experimental Control over the Behavioral Repertoire

(A and B) Schematic (A) of a virtual reality experiment in which the mouse runs on a spherical treadmill while viewing a monitor that provides visual-flow feedback. Example traces (B) of neural Ca^{2+} activity (black $\Delta F/F$ traces) from a layer 2/3 visual cortical neuron, during running with visual-flow feedback (feedback session), and during running with visual stimulation that was unrelated to the mouse's motion (playback sessions). Baseline periods, when the animal was sitting without visual flow, are unshaded. Periods shaded in gray are those when the mouse was running and received visual-flow feedback. Orange denotes periods when the animal was running but there was a feedback mismatch (no visual flow). Green denotes playback periods, when the animal was sitting while viewing visual flow. Both panels are adapted from Keller et al. (2012).

(C) Photograph of a virtual reality setup. Adapted from Dombeck et al. (2010).

(D and E) Two-photon image (D) of GCaMP3-expressing layer 2/3 neurons in parietal cortex. Ca^{2+} activity traces (E) from the 3 cells circled in (D), recorded while the animals performed a T-maze task. Both panels are adapted from Harvey et al. (2012).

(F and G) Comparisons of place cell activity (F) between virtual (red) and real (blue) linear tracks. Activation ratio (left) and firing rates (right) of cells active on the track and at the goal location. Comparison (G) of place cell activity on a real (blue) and virtual (red) linear track regarding the spatial information content in the cells' spiking patterns. Spatial information content across 432 cells active on a virtual linear track was significantly lower than in 240 cells active on a real-world linear track. Both panels are adapted from Ravassard et al. (2013).

sets with comparable numbers of individual cells there will need to be noteworthy improvements in imaging speed, field of view, and reduction of fluorescence background.

Optical Imaging Paradigms for Studies in Behaving Animals

Two complementary paradigms have emerged for optical brain imaging studies in behaving mammals: those involving head-fixed animals (Figure 3) and those permitting unconstrained behavior (Figure 4). Depending on the scientific question, limiting an animal subject's range of behavior can be a benefit or a drawback. Both approaches are likely to play important, ongoing roles in the study of cellular and neural circuit dynamics during active animal behavior. Genetically encoded Ca^{2+} indicators and chronic animal preparations have allowed time-lapse Ca^{2+} imaging studies across weeks in both head-fixed and freely behaving rodent preparations. This has permitted long-term tracking of ensemble neural dynamics, such as for studies of learning and memory (Huber et al., 2012; Keck et al., 2013; Masamizu et al., 2014; Peters et al., 2014; Ziv et al., 2013).

The groundwork for these recent studies was set in part by the substantial history of experiments that used voltage-sensitive dyes or intrinsic optical effects to probe population-level neural dynamics in awake head-restrained monkeys (Grinvald et al., 1991; Raffi and Siegel, 2005; Seidemann et al., 2002; Tanigawa et al., 2010), as well as freely moving (Ferezou et al., 2006) and
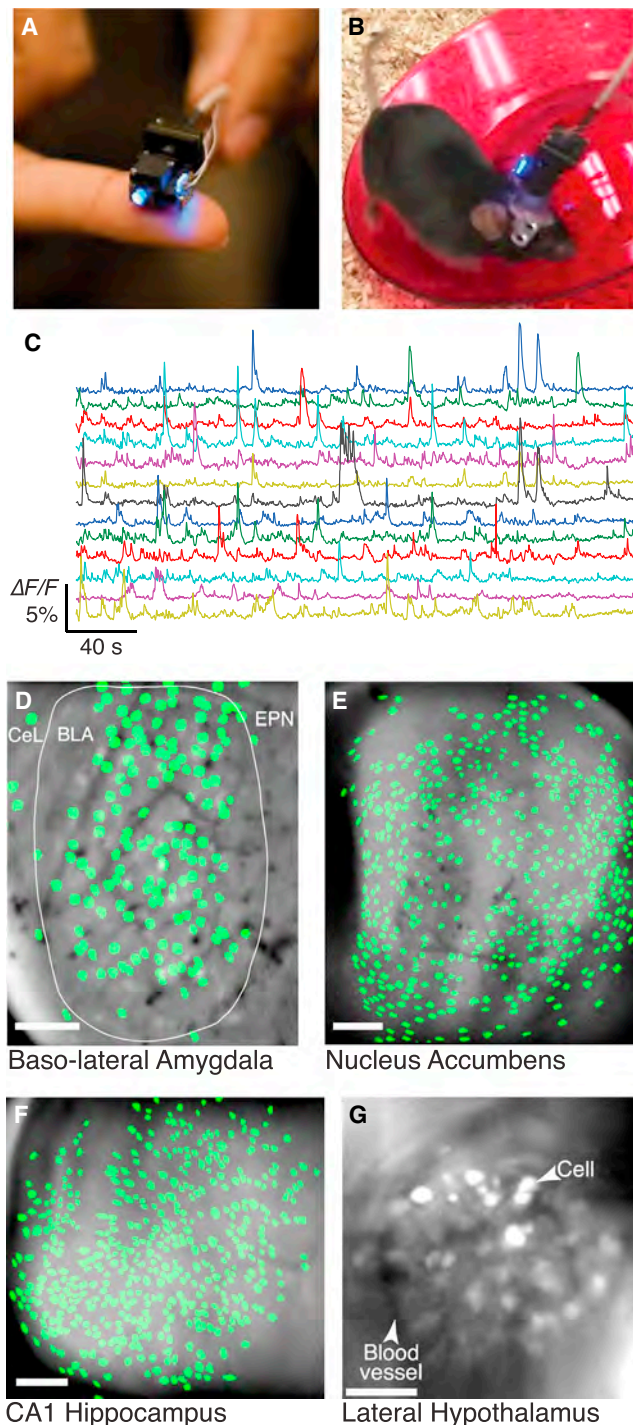
Figure 4. Head-Mounted Microscopes Based on Miniaturized Optical Components Allow Brain Imaging in Freely Behaving Animals
(A) Photograph of the miniaturized integrated microscope (Ghosh et al., 2011).
(B) Photograph of a mouse running on a wheel as the integrated microscope captures Ca^{2+}-related fluorescence signals.
(C) Ca^{2+} activity traces from 10 cells acquired in the mouse basolateral amygdala using the integrated microscope. Cell filters used to calculate the traces were extracted from the Ca^{2+} imaging data using a cell-sorting method based on principal and independent component analyses (Mukamel et al., 2009).

head-fixed rodents (Ferezou et al., 2007; Kuhn et al., 2008; Mohajerani et al., 2013, 2010; Zhang et al., 2012). To date, nearly all cellular level fluorescence imaging studies in behaving animals have used Ca^{2+} indicators. The recent improvements in voltage indicators (Figure 2) and demonstrations in head-restrained mice with new reporters of glutamate (Marvin et al., 2013) and monoamine (Muller et al., 2014) release indicate that the set of fluorescent sensors usable in behaving animals is now poised for expansion.

The head-fixed format for optical brain imaging allows the use of conventionally sized optical instrumentation, typically a two-photon microscope residing on a vibration-isolation table (Chen et al., 2013b; Dombeck et al., 2009; Dombeck et al., 2010, 2007; Harvey et al., 2012; Kaifosh et al., 2013; Keck et al., 2013; Keller et al., 2012; Lecoq et al., 2014; Lovett-Barron et al., 2014; Masamizu et al., 2014; Miller et al., 2014; Nimmerjahn et al., 2009; Peters et al., 2014; Petreanu et al., 2012). This differs from studies in freely moving animals, which require miniaturization of the entire or part of the microscope so that the animal can carry it on the cranium during unrestrained behavior. The conventional high-performance objective lenses that are permissible in the head-restrained format, combined with the optical sectioning afforded by two-photon imaging, allow activity in dendrites, or even in fine structures such as axonal boutons and dendritic spines, to be detected during active behavior (Boyd et al., 2015; Kaifosh et al., 2013; Marvin et al., 2013; Petreanu et al., 2012; Sheffield and Dombeck, 2015; Xu et al., 2012). It is also relatively straightforward to perform two-color fluorescence imaging, such as for distinguishing within a broad population of indicator-labeled cells the activity of a dual-labeled subset, defined genetically or by its connectivity (Chen et al., 2013b; Inoue et al., 2015). With the help of microendoscopes or microprisms that can be inserted into the live brain, a variety of viewing angles and deep brain areas can be optically accessed that would be otherwise prohibitive (Andermann et al., 2013; Barretto et al., 2009, 2011; Chia and Levene, 2009; Heys et al., 2014; Jung et al., 2004; Jung and Schnitzer, 2003; Levene et al., 2004; Low et al., 2014). Head fixation also eases certain auxiliary manipulations, such as a mid-session intracranial drug delivery or visually guided electrical recording (Lovett-Barron et al., 2014; Nimmerjahn et al., 2009). Further, as new optical hardware or imaging techniques emerge, head-restrained

(D) Map of 162 cell bodies identified in the mouse basolateral amygdala (BLA) within Ca^{2+} imaging data acquired with the integrated microscope, overlaid on an image of the mean fluorescence. CeL, centrolateral nucleus of the amygdala; EPN, endopiriform nucleus.
(E) Map of 555 cell bodies identified in the mouse nucleus accumbens within Ca^{2+} imaging data acquired with the integrated microscope, overlaid on an image of the mean fluorescence.
(F) Map of 472 cell bodies identified in the mouse hippocampal area CA1 within Ca^{2+} imaging data acquired with the integrated microscope, overlaid on an image of the mean fluorescence.
(G) Fluorescence image of GCaMP6m expression in the lateral hypothalamus, acquired with the integrated microscope. Arrows indicate a GABAergic neuron expressing GCaMP6m and a blood vessel.
Scale bars are 100 μm in (D)–(G). (A) and (B) are courtesy of Kunal Ghosh and Inscopix Inc.; (C) and (D) were provided by Benjamin F. Grewe; (E) was provided by Jones G. Parker and Biafra Ahanonu. (F) is courtesy of Lacey J. Kitch, Margaret C. Larkin, and Elizabeth J.O. Hamel. (G) is courtesy of Garret Stuber and is adapted from Jennings et al. (2015).

animal behaviors facilitate the prompt application of these approaches to in vivo brain imaging, without the prerequisite of first creating a miniaturized version suitable for mounting on a freely moving animal; this advantage is especially notable for techniques involving complicated optical setups.

Initial Ca^{2+} imaging studies in awake head-restrained rodents involved relatively simple behaviors such as quiet wakefulness (Bathellier et al., 2012; Greenberg et al., 2008; Kato et al., 2012; Kuhn et al., 2008; Mohajerani et al., 2010) and grooming or locomotion (Dombeck et al., 2009,2007; Nimmerjahn et al., 2009). Behavioral assays have since progressed, making use of the head-fixed preparation's suitability for controlled delivery of sensory stimuli (Andermann et al., 2011; Blauvelt et al., 2013; Carey et al., 2009; Miller et al., 2014; Patterson et al., 2013; Verhagen et al., 2007). The addition of a trained behavioral response enabled studies of perceptual discrimination tasks (Andermann et al., 2010; Komiyama et al., 2010; O'Connor et al., 2010). A version of associative fear conditioning even exists for brain imaging in head-restrained animals (Lovett-Barron et al., 2014). For studies of motor behavior, the study of many stereotyped behavioral trials can be vital, and the constraints of head fixation can facilitate this stereotypy (Huber et al., 2012; Masamizu et al., 2014; Peters et al., 2014).

Brain imaging in head-restrained animals also allows the use of virtual reality approaches (Harvey et al., 2009; Hölscher et al., 2005) (Figures 3A–3C), which enable sensory manipulations that would be difficult or impossible to achieve in freely behaving animals. For instance, one can create artificial mismatches between an animal's motor behavior and the visual feedback signals it receives in response (Figures 3A and 3B) (Keller et al., 2012). Virtual reality approaches have also allowed imaging of neural activity related to spatial navigation behaviors (Figures 3D and 3E) (Dombeck et al., 2010; Harvey et al., 2012) that have usually been studied in freely moving animals (Hafting et al., 2005; O'Keefe and Dostrovsky, 1971; Ziv et al., 2013). Researchers are still exploring the extent to which neural responses during virtual-navigation tasks in restrained animals mimic those occurring during normal unrestrained navigation (Aronov and Tank, 2014; Ravassard et al., 2013). Even if visual aspects of the virtual reality are highly convincing, there might be key differences in head direction, self-motion, vestibular and olfactory cues, which might in turn impact neural coding (Figures 3F and 3G). Continued study of these issues and innovation of new virtual reality methods (Aronov and Tank, 2014; Sofroniew et al., 2014) will help expand and define the set of scientific questions that can be fruitfully examined by brain imaging in head-fixed animals.

Complementary to techniques that require head fixation, optical approaches that involve miniaturized head-mounted imaging devices and flexible tethers (fiber optics or floppy electrical lines) enable brain-imaging studies in freely moving mammals (Figures 4A and 4B). This capability is important, because some animal behaviors are incompatible with or poorly adapted to head-restrained conditions. Examples include the social behaviors such as fighting, mating, care-giving, and other forms of interaction; behaviors probing stress or anxiety that might be influenced by the stress of head restraint; motor behaviors involving motion of the head and neck; olfactory behaviors

involving active exploration of an odor landscape; and vestibular-dependent behaviors. Miniaturized optical devices for use in freely moving animals are also generally compatible with the wide set of behavioral assays and apparatus already deployed and validated across neuroscience research and in the neuropharmaceutical industry, including for studies of operant, navigation, social, learning, sensory, and motor behaviors.

Initial innovation of head-mounted devices for imaging cellular activity in behaving rodents focused on miniaturized laser-scanning two-photon microscopes, all of which used fiber optics to deliver ultrashort-pulsed laser illumination to the microscope (Engelbrecht et al., 2008; Flusberg et al., 2005; Göbel et al., 2004; Helmchen et al., 2001; Piyawattanametha et al., 2009; Sawinski et al., 2009). The requirements of a miniaturized laser-scanning system imposed some challenging engineering design tradeoffs. The aim of reducing the size and mass of the head-mounted components, including the scanning apparatus, conflicted with the desire to scan a broad field of view at adequate frame rates. Miniaturized two-photon microscopes that were in principle sufficiently small (∼0.6–3.9 g in mass) for use in freely behaving mice never progressed in practice beyond studies in anesthetized mice (Engelbrecht et al., 2008; Flusberg et al., 2005; Göbel et al., 2004; Piyawattanametha et al., 2009). The challenge of miniaturization is less severe for studies in rats. One study successfully demonstrated two-photon Ca^{2+} imaging in visual cortical neurons of freely behaving rats using a 5.5 g microscope that contained a miniaturized scanning mechanism, allowing a mean of 16 neurons to be monitored per behaving animal (11 Hz frame rate) (Sawinski et al., 2009). An alternative strategy of scanning the laser illumination before it entered a fiber optic bundle compromised optical performance and mechanical flexibility of the tether to the animal (Göbel et al., 2004). To date, the combined engineering challenges of fiber-optic delivery of ultrashort laser pulses and laser-scanning in a miniaturized two-photon microscope remain sufficiently complex that no studies using this approach in freely behaving animals have been published in the last few years.

To circumvent these challenges while achieving broader fields of view and faster frame rates, recent work on miniaturized microscopes has focused on camera-based, one-photon epifluorescence microscopes that are sufficiently lightweight (∼1.1–1.9 g) for use in freely behaving mice (Flusberg et al., 2008; Ghosh et al., 2011). The success of the one-photon approach for Ca^{2+} imaging in freely moving animals is in large part due to the substantial signaling dynamic range of recent Ca^{2+} indicators. Even in the absence of the optical sectioning provided by two-photon imaging, this signaling dynamic range is what makes excellent d' values possible in the face of substantial background photon flux and Ca^{2+} signals from neural elements outside the focal plane. Initially, the illumination and fluorescence image propagated to and from the mouse via a fiber-optic bundle (Flusberg et al., 2008; Murayama and Larkum, 2009; Murayama et al., 2007, 2009; Soden et al., 2013), but the subsequent approach of integrating all optical components within the head-mounted device has proven notably superior regarding the optical sensitivity, field of view, resolution, mechanical flexibility for the animal, and portability between experimental sites that can be attained (Ghosh et al., 2011).

Using a fingertip-sized integrated microscope (Figure 4A) that combines a blue light-emitting diode (LED), a cell phone CMOS camera chip for digital imaging, miniaturized lenses, and a fluorescence filter set within a single compact housing, one-photon imaging of neural Ca^{2+} signals in freely behaving mice has become more widespread since the initial experiments (Figures 4B–4F) (Berdyyeva et al., 2014; Ghosh et al., 2011; Jennings et al., 2015; Ziv et al., 2013). The integrated microscope has a $\sim$0.5 mm^2 field of view (Ghosh et al., 2011), which permits dense sampling of up to $\sim$1,000 individual neurons simultaneously (Alivisatos et al., 2013; Chen et al., 2013a; Ziv et al., 2013), about 20–50 times more cells than can be individually monitored in behaving mice using electrophysiological methods. For comparison, tabletop two-photon microscopes have also recorded Ca^{2+} transients from $\sim$1,000 cells at a time, but to date only at slow frame acquisition rates of 0.1–0.5 Hz due to speed limitations set by raster-scanning the laser excitation (Stirman et al., 2014). In freely moving rats, multi-electrode recordings can monitor up to $\sim$250 neurons concurrently, (Pfeiffer and Foster, 2013), much closer to the $\sim$1,000 cell tallies feasible by imaging.

The first Ca^{2+} imaging studies with the integrated microscope were acute experiments that compared the complex spiking dynamics of up to $\sim$200 individual Purkinje neurons in the cerebellar cortex across different motor behavioral states (Ghosh et al., 2011). By combining the integrated microscope with a microendoscope for imaging deep brain areas (Jung et al., 2004; Jung and Schnitzer, 2003; Levene et al., 2004) and a chronic preparation for time-lapse microendoscopy (Barretto et al., 2011), a subsequent study examined the long-term dynamics of the mouse hippocampal ensemble neural representation of space (Ziv et al., 2013).

Currently ongoing studies with the integrated microscope involve time-lapse imaging of ensemble neural Ca^{2+} dynamics in other brain regions such as the striatum, nucleus accumbens, hypothalamus, dentate gyrus, substantia nigra, amygdala, neocortex, and the ventral tegmental area (e.g., Figures 4C–4F). Unlike conventional two-photon microscopes, which can resolve dendrites and other structures $\sim$500–700 μm below the surface of the brain, using one-photon microscopy one can detect and extract cellular signals $\sim$150–200 μm deep into tissue, and further if the cell labeling is sparse. However, the combination of the integrated microscope and various microendoscopes (typically 1,000–500 μm in diameter; up to $\sim$8 mm long) has proven surprisingly versatile in examining brain areas never before imaged optically in live mammals (Jennings et al., 2015). By adding a microprism to the tip of the microendoscope to form a periscope probe (Murayama and Larkum, 2009; Murayama et al., 2007, 2009), or using a microprism in direct combination with the microscope (Andermann et al., 2013; Chia and Levene, 2009; Heys et al., 2014; Low et al., 2014), still more brain areas and anatomical views will be accessible in freely behaving mice.

In addition to enabling large-scale Ca^{2+} imaging during active mouse behavior, the permanent optical alignment and compatibility with existing behavioral apparatus have been key attractions of the integrated microscope. The microscope can be readily used in animal housing facilities and combined with existing behavioral chambers such as mazes or operant conditioning boxes. Floppy electrical lines to the mouse's head exert scant mechanical influence on the animal and transmit high-definition (HD) digital video directly to a data acquisition system. These virtues make it feasible to study several mice in parallel, each wearing an integrated microscope, facilitating the acquisition of data sets with sufficient statistical power to address sophisticated questions about ensemble neural coding.

Collectively, brain-imaging studies in head-restrained and freely behaving animals are becoming widespread for addressing questions of many kinds. In our laboratory, we use both approaches and allow the scientific question to guide the decision of which imaging format is preferred. With continued innovation, we expect both formats will attain additional capabilities (see Outlook), such as concurrent imaging of multiple brain areas and increases in the number of cells that can be monitored (Lecoq et al., 2014; Stirman et al., 2014), expanded capabilities for volumetric or multi-plane imaging (Bouchard et al., 2015; Quirin et al., 2014; Sheffield and Dombeck, 2015), and sophisticated combinations of imaging with optogenetic manipulations (Hochbaum et al., 2014; Packer et al., 2015; Prakash et al., 2012; Rickgauer et al., 2014).

Computational Image Analyses

Imaging data on the dynamics of large sets of individual neurons typically undergo multiple stages of computational processing. First, there are housekeeping operations, such as image registration to correct for displacements due to brain motion. Second, there is cell sorting, in which one extracts from the video data the fluorescence signals from the individual neurons. Third, one may opt to convert the continually varying fluorescence time traces into digitized event rasters of neural activity, at least when it is feasible to do so. Finally, there are the specific statistical analyses that probe the particular biological questions at issue in the experiment. We consider here the first three stages, which are of general interest since they apply to the majority of Ca^{2+} imaging studies presently underway in behaving mammals.

A first stage of analysis focusing on image registration is greatly aided by having a high-quality animal preparation for stable in vivo imaging. With sufficient care to surgical procedures and mechanical damping of brain motion during imaging, a rigid image registration usually suffices to align the different video frames of a Ca^{2+} imaging data set to a precision adequate for subsequent analyses (Thévenaz et al., 1998; Ziv et al., 2013). Some authors have also registered the individual lines or pixels within single image frames (Dombeck et al., 2007; Greenberg and Kerr, 2009).

For a second stage of analysis focused on cell sorting, there are several approaches in common usage. In all likelihood, none of these algorithms will be adequate to fully address the needs for cell sorting imposed by the large-scale Ca^{2+} imaging data sets containing $\sim$10^3–10^5 individual neurons that are now emerging (see Outlook) (Alivisatos et al., 2013; BRAIN Initiative, 2014; Freeman et al., 2014). One widespread and elementary method for separating signals from different cells is to demarcate the boundaries of individual cells and denote each enclosed area as a region of interest (ROI), one for each cell (Dombeck et al., 2007; Göbel et al., 2007; Kerr et al., 2005; Kuchibhotla

et al., 2014; Lovett-Barron et al., 2014; Ozden et al., 2008; Peters et al., 2014).

Although conceptually simple, this approach has multiple drawbacks, largely because the boundaries of individual cells are almost never commensurate with the boundaries between image pixels or voxels. Even pixels that seem to be in the middle of a cell body can contain contaminating Ca^{2+} signals from neuropil activation, such as from synaptic contacts or out-of-focal-plane structures. Especially with the dense indicator labeling that is typical of large-scale Ca^{2+} imaging studies, many image pixels may contain multiple sources of Ca^{2+} signals, including neuropil, somata, dendrites, and axons (Kerr et al., 2005; Mukamel et al., 2009), thereby introducing cross talk. In addition to the sheer density of neuropil, which makes such cross talk likely, aspects of the imaging setup such as resolution, optical sectioning, and susceptibility to light scattering deep in tissue also strongly influence concerns about cross talk. Concerns about cross talk are especially warranted for one-photon imaging data, as cells' boundaries usually appear blurred or distorted, and Ca^{2+} signals from neural elements outside the focal plane can contaminate the activity traces of cells encircled within ROIs. Cognizant of these issues, some researchers draw very conservative boundaries for cell bodies, by keeping the ROI perimeter well inside the pixels that actually contain the cell body membrane. Unfortunately, this workaround discards many useful signal photons arising near the cell perimeter, because the cytoplasmic volume of a bounded ROI scales cubically with its radius. This in turn can compromise d' values. This workaround also cannot eliminate Ca^{2+} signal contaminants from neuropil that may corrupt pixels near the soma center. For this reason some researchers try to remove centrally located contaminants from the ROI signals by subtracting a weighted, time-varying trace representing the neuropil's Ca^{2+} activity; unfortunately, the choice of the weight is typically ad hoc. For studies of fine neural structures such as dendrites, the workaround is even hard to execute unless the fluorescence labeling is very sparse. Needless to say, manual approaches to defining ROIs are nearly prohibitive with the data sets of ∼1,000 individual cells that are becoming increasingly common in mammals, but versions with some computer-assisted image segmentation remain feasible to perform (Ohki et al., 2005). Nevertheless, computer-assisted drawing of ROIs as a means of cell sorting typically relies upon heuristic definitions of cell morphology rather than generally applicable statistical principles for decomposing a data set into its constituent signal sources.

In comparison to cell-sorting methods based on cell morphology, another class of sorting approaches relies on the spatiotemporal attributes of neurons' activity patterns (Dombeck et al., 2010; Maruyama et al., 2014; Miri et al., 2011; Mukamel et al., 2009; Ozden et al., 2008). For instance, one such approach involves a linear regression of image pixels' fluorescence time series against the animal's sensory inputs or behavioral outputs (Miri et al., 2011). This approach may work well in some circumstances but is not general purpose, since it is limited to cells with significant linear correlations to the specific sensory or behavioral parameters chosen for the regression and requires an image segmentation step to isolate the individual cells from an image of the pixels' regression significance levels. It does not explicitly address the issues of cross talk noted above, nor does an approach that groups pixels with correlated fluorescence time traces (Ozden et al., 2008).

One cell-sorting method that is expressly formulated to disentangle signals between different cellular elements involves first a principle component analysis (PCA), for purposes of dimensionality reduction, followed by an independent component analysis (ICA) that seeks the set of independent Ca^{2+} signal sources (Brown et al., 2001; Hyvärinen and Oja, 2000; Mukamel et al., 2009). Many neuroscientists are familiar with the capabilities of ICA for blind source separation and cross talk removal in the context of the "cocktail party problem" (Bell and Sejnowski, 1995), which involves separating the speech signals from different people in a crowded room of speakers. The ICA approach to cell sorting makes no assumptions about cells' morphologies but does posit that cells' signals are statistically sparse and mutually independent (Mukamel et al., 2009). Notably, image analysis by ICA is well known in multiple contexts to be robust to modest levels of motion artifact and violations of the assumption of independence (McKeown et al., 1998; Mukamel et al., 2009; Reidl et al., 2007). For instance, when applied to Ca^{2+} imaging movies of complex spiking activity from cerebellar Purkinje neurons, the ICA approach correctly identified individual cells unless their pair-wise correlation coefficients rose above ∼80%; at higher levels of synchronous activity, cell pairs were assigned a single independent component that could be correctly split into two via an additional image segmentation step (Mukamel et al., 2009). This degree of robustness and explicit handling of cross talk has made the ICA approach broadly applicable to Ca^{2+} imaging studies of many different cell types (e.g., Figure 4), conducted with one- and two-photon fluorescence imaging (Dombeck et al., 2010; Ghosh et al., 2011; Mukamel et al., 2009; Ziv et al., 2013), and the software is available in open-source and commercial forms. ICA can also pick out dendritic Ca^{2+} signals from densely labeled tissue in an automated way (Lecoq et al., 2014; Xu et al., 2012). Approaches based on non-negative matrix factorization have also shown promising initial capabilities for identifying dendritic activity and merit further exploration (Maruyama et al., 2014).

Nevertheless, when cells are densely labeled with the Ca^{2+} indicator, all sorting methods that represent individual cells as spatial filters face basic tradeoffs between signal fidelity and cross talk reduction. This limitation pertains to both the ICA- and ROI-based approaches. Thanks to recent improvements in Ca^{2+} indicators (Chen et al., 2013c), in vivo Ca^{2+} imaging reveals a greater portion of neural activity than ever before, so Ca^{2+} imaging data sets from densely labeled tissue are increasingly testing the limits of what spatial filtering approaches to cell sorting can achieve. Future work in this area will very likely need to move beyond the use of spatial filters.

After extraction of individual cells and their fluorescence time traces from the video data sets, in a third stage of analysis one may further seek to identify the discrete incidences of each cell's activation and express these as a digitized train of events or spikes. Not all Ca^{2+} imaging experiments require or allow this, such as when examining fast-spiking interneuron dynamics (Kerlin et al., 2010; Runyan et al., 2010). When discrete activation events are apparent in the fluorescence traces, the Ca^{2+}

transients often have an approximately stereotyped waveform within a given cell class, and different algorithms for spike detection make use of this stereotypy in different ways. Ca^{2+} transients often exhibit a fast rise followed by an exponential decay, and by using a specific temporal filter that aims to capture this waveform in how it stands out from noise fluctuations, deconvolution-based methods identify when the temporally filtered version of the fluorescence trace crosses a detection threshold (Holekamp et al., 2008; Vogelstein et al., 2010; Yaksi and Friedrich, 2006). Other spike detection approaches use template matching (Kerr et al., 2005) or likelihood estimates of spike incidences based on the fluorescence waveform (Wilt et al., 2013), including in an iterative manner that aims to remove Ca^{2+} transients successively from the fluorescence trace until only noise remains (Grewe et al., 2010; Wilt et al., 2013). In cell types that fire bursts of action potentials, individual spikes sometimes cannot be resolved within the temporally low-pass-filtered signals provided by the Ca^{2+} indicator. In these cases it may be desirable to detect spike bursts as single events. The variability in the Ca^{2+} bursts precludes assumptions of a stereotyped optical waveform, but the application of a simple detection threshold can nevertheless be highly effective (Ziv et al., 2013).

Spike detection algorithms based on supervised learning methods typically require simultaneously acquired optical and electrophysiological recordings of the very same cells, from which one trains the algorithm to recognize neural activation events (Greenberg et al., 2008; Sasaki et al., 2008). Of note, even within one cell type, Ca^{2+} transients observed in vitro during paired recordings used for training may differ in their signal and noise characteristics from what is seen in vivo. However, paired optical and electrophysiological recordings of cellular activity in live animals are often technically challenging; in cases when they are feasible, the resulting data sets generally provide an excellent check on the entire analysis pipeline for in vivo Ca^{2+} imaging (Greenberg et al., 2008; Grewe et al., 2010; Kerr et al., 2005; Mukamel et al., 2009).

On the whole, it has been our experience that cell sorting is the analysis step at which the greatest performance differences arise between algorithms in common use. By comparison, different algorithms for extracting spikes from fluorescence traces do disagree in some of their decisions about individual candidate spikes, but in many experiments the extent of these disagreements is insufficient to alter the eventual biological conclusions. To this point, paired optical and electrical recordings have revealed spike detection accuracies of ∼85%–95% for several algorithms (Greenberg et al., 2008; Grewe et al., 2010; Mukamel et al., 2009). Signal detection theory provides another means of evaluating the multi-step computational procedure that converts the raw Ca^{2+} imaging data into neural spike trains. Due to the substantial non-stationary noise sources in studies of live animals, one generally cannot attain the physical limit on spike detection as set by optical shot noise. Nevertheless, having this limit remains useful for gauging the efficacy of computational approaches across different optical setups.

Outlook

The approaches discussed here for cellular imaging in behaving mammals are all relatively young, and we expect exciting further

developments of multiple kinds. For starters, we foresee expansion in the aspects of neural activity that can be visualized, using improved voltage indicators and reporters of neurochemical signaling (Marvin et al., 2013; Muller et al., 2014). Improved voltage indicators will likely make imaging of single action potentials possible in behaving mammals with millisecond-scale accuracy of spike timing estimation. Voltage imaging of sub-threshold membrane potential oscillations in genetically specified neurons should also be feasible, at least when aggregating signals over multiple cells, and might fruitfully be combined with Ca^{2+} imaging of individual cells' spiking patterns, to observe spiking and oscillatory rhythms concurrently.

We also expect an expansion in the range of mammalian species in which cellular level imaging is feasible during active animal behavior. Nearly all cellular imaging studies published to date in behaving mammals have used rodents. Several research groups are pursuing two-photon Ca^{2+} imaging as a means of monitoring large ensembles of individual neurons in awake, head-restrained monkeys. Challenges include attaining suitable patterns of indicator expression, minimizing image artifacts due to brain movements that are larger than those in rodents, and achieving adequate optical penetration into brain tissue to reach the neurons of interest. The combination of miniature microscopes and microendoscopes might help in addressing the latter two issues, by providing an optical conduit that can interrogate cells far beneath the brain surface and that moves to a certain extent with the surrounding brain tissue. The primate cranium is sufficiently big to accept multiple miniature microscopes, potentially allowing imaging of several brain areas in parallel. As the marmoset primate model grows in prominence (Cyranoski, 2014), we expect analogous imaging approaches to arise for this species as well.

Another likely set of advancements in cellular level imaging will involve further integration with other optical technologies. Through the development of spectrally compatible sets of neural activity indicators and optogenetic actuators (Hochbaum et al., 2014; Prakash et al., 2012), it is now feasible to both image and manipulate spiking dynamics during active animal behavior (Packer et al., 2015; Rickgauer et al., 2014). Combining fluorescence imaging and optogenetic manipulation in a single field of view requires ensuring that the optical wavelengths used for the two techniques do not induce cross talk effects. Optical techniques for shaping three-dimensional patterns of illumination may be particularly useful for confining light delivery to chosen subsets of cells (Anselmi et al., 2011; Bègue et al., 2013; Nikolenko et al., 2013; Packer et al., 2012, 2015; Quirin et al., 2014; Reutsky-Gefen et al., 2013), which could help minimize any cross talk and enable sophisticated experiments in which optogenetic control is restricted to cells whose dynamics show specific coding properties or relationships to animal behavior, as determined by in vivo imaging.

Eventually, it may even be possible to perform these selective manipulations in a closed-loop manner, e.g., influencing a subset of cells with particular coding properties in a manner that depends directly on the time-dependent dynamics of either the animal's behavior or another (potentially overlapping) subset of cells. Both versions of such closed-loop experimentation would likely benefit from fast computational methods for analyzing the

neural imaging data, to identify cells with particular coding properties in the midst of an experimental session. Real-time extraction of Ca^{2+} signals from the ROIs of up to 11 neurons in behaving mice has already been demonstrated (Clancy et al., 2014), although not yet combined with optogenetics. Real-time computational capabilities for extracting the dynamics of greater numbers of cells will surely appear in the upcoming future.

Cellular level in vivo imaging studies also stand to benefit from combination with *post mortem* methods of whole brain or brain sample tissue clearing, which enable high-resolution fluorescence imaging of cells preserved in the tissue's intact three-dimensional form (Chung et al., 2013; Hama et al., 2011; Helmchen et al., 2013; Susaki et al., 2014; Tomer et al., 2014; Yang et al., 2014). By examining the same cells' activity patterns during active animal behavior and then *post mortem* their patterns of protein expression and anatomical connectivity, neuroscientists will gain new understanding of how neural dynamics relate to macromolecular content and neural circuit structure.

Through another set of advances we expect the scalability and throughput of imaging approaches in behaving mammals to improve. For instance, it may be possible to conduct cellular level imaging studies of multiple freely moving mice in parallel, with minimal human supervision. The integrated microscope naturally lends itself to this kind of scalability, since it is based on mass-fabricated optoelectronics. Although imaging in multiple mice is already possible today at a modest scale, the full realization of this paradigm might require wireless modes of video transmission, so that animals could provide data for longer periods without human supervision. Wireless electrophysiological recordings from multiple animals in parallel are already widely used in behavioral neuropharmacology studies, and a wireless approach to cellular imaging might notably benefit preclinical and therapeutic discovery efforts. To date, brain imaging in freely moving mice has been combined with wireless telemetry systems that transmit electroencephalography (EEG) and electromyography (EMG) signals (Berdyyeva et al., 2014). There have also been efforts to improve the throughput of imaging studies in head-restrained rats, by allowing rats to initiate brief periods of voluntary head restraint underneath the objective lens of a conventional two-photon microscope (Scott et al., 2013). Along with hardware advances to increase throughput, improved computational methods would be crucial to handle the barrage of data that a truly high-throughput approach would produce.

The process of sorting individual neurons and their dynamics from Ca^{2+} imaging data has already become increasingly nontrivial as data sets have grown in magnitude. For instance, a day's worth of Ca^{2+} imaging in freely behaving mice can easily yield a few terabytes of raw data, which can consume another full workday for image pre-processing and cell sorting. In addition to increases in computational speed, algorithmic progress will likely also be important for improved cell sorting. The recent gains in Ca^{2+} indicator performance have, in certain respects, made separation of the different neural sources of Ca^{2+} activity more challenging, since at any instant in time there is a greater likelihood that neighboring somata, dendrites, and neuropil will appear as simultaneously active. With prior less sensitive Ca^{2+} indicators a greater portion of neural activity was invisible,

making it easier to identify the sparser visible patterns of activation. Of course, the superior *d'* values provided by the newer indicators partially counteract this effect. Nevertheless, we expect increasing needs for cell-sorting algorithms that can detect various facets of cellular and sub-cellular activity in densely labeled tissue, and in a computational time that scales reasonably with the amount of data (Freeman et al., 2014). As noted in the NIH BRAIN report, neuroscientists and statisticians will likely need to work together toward proper analysis and interpretation of the emerging large data sets from optical studies (BRAIN Initiative, 2014). The involvement of computer scientists will likely also be critical for algorithm design and implementation, as well as database design and management.

In addition to the areas of potential progress noted above, which generally concern issues ancillary to the optics of image formation, another set of likely advances will involve strides in the optical imaging process itself. Future forms of microscopy will likely provide superior capabilities for imaging the dynamics of large sets of individual neurons in behaving animals over extended three-dimensional (3D) volumes, at further depths in tissue from the objective lens, at faster acquisition rates, and across multiple brain areas and greater numbers of cells. For these pursuits the systems engineering approach will be critical for guiding and coordinating all aspects of innovation in a holistic way.

For instance, the challenge of attaining fast imaging of neural activity over extended 3D volumes involves considerations of more than just fast cameras or fast 3D-scanning methods. The fundamental limitations to detection of neural activity are set by photon statistics, and a substantial increase in the number of voxels that must be sampled per unit time poses a serious test of how to achieve adequate photon counts and *d'* values while maintaining the overall time resolution. As an illustration, a laser-scanning microscope that achieves satisfactory photon counts when serially scanning an image plane of 512 × 512 pixels in a time, *T*, will suffer a precipitous, ∼23-fold decline in *d'* values if one uses the same serial scanning parameters to sample a volume of 512 × 512 × 512 voxels in time *T* under otherwise equal optical conditions.

Similar considerations apply when considering the design of new microscopy modalities for high-speed voltage imaging, monitoring greater numbers of neurons, or observing multiple brain areas in parallel using a single laser source. Regardless of whether one seeks to maintain the same field of view but increase the image acquisition rate, scan a broader field of view and hence more neurons using a large objective lens, or divide the illumination into two or more beams that each scan a distinct brain area (Lecoq et al., 2014), the fundamental considerations regarding detection of neural activity concern how to attain satisfactory *d'* values. In addition to framing the common nature of the problem due to limited photon counts, signal detection theory suggests possible solutions. As noted above, spike detection can succeed well with limited numbers of signal photons provided that the background fluorescence is extremely low. Thus, it is possible that a major advance in fast volumetric imaging might come via further progress in indicator development. There are also other possible routes to high-speed imaging in behaving animals that merit equal consideration.
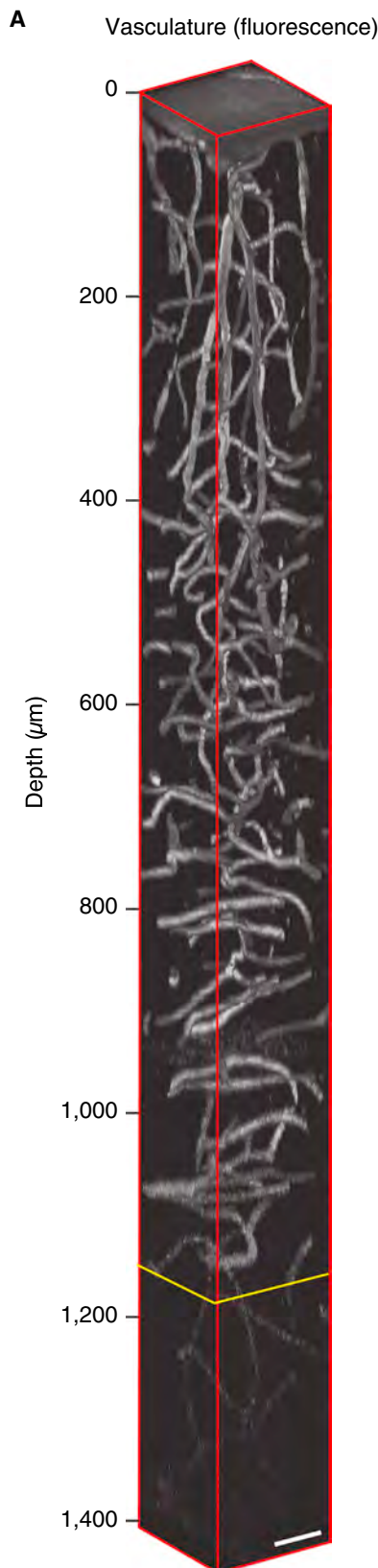
A

Vasculature (fluorescence)

Figure 5. Three-Photon Fluorescence Imaging Penetrates Deeply into Brain Tissue
(A) A reconstructed 3D volume of fluorescently labeled microvasculature imaged in a live mouse using three-photon fluorescence microscopy. The volume extends ventrally from the neocortical surface down into CA1 hippocampus. Scale bar, 50 μm. Adapted from Horton et al. (2013).

For example, acousto-optic methods of fast 3D laser-scanning allow random-access scanning patterns, in which only a subset of voxels of interest is sampled, and can sharply increase the sampling duration per voxel as compared to a raster-scan of the total volume of interest (Duemani Reddy et al., 2008; Grewe et al., 2010; Katona et al., 2012). Although acousto-optic scanners have some intricate optical drawbacks, one simple drawback when studying behaving mammals is that random-access scanning approaches neither are robust to brain motion nor produce data sets conducive to image alignment. Other possible avenues to fast volumetric imaging involve sampling of multiple voxels in parallel. Candidate imaging modalities include light sheet microscopy, which samples entire planes in the specimen with each camera frame acquisition (Ahrens et al., 2013; Holekamp et al., 2008); light field microscopy, which samples multiple specimen planes concurrently (Broxton et al., 2013; Levoy et al., 2009; Prevedel et al., 2014); and scanless approaches to two-photon imaging that sample in parallel a selected subset of voxels (Quirin et al., 2014; Watson et al., 2010). To work well in optically scattering brain tissue of behaving mammals, all of these candidates would likely require accompanying innovations in data analysis.

More generally, light scattering imposes key limitations on the optical penetration depth into the mammalian brain that can be achieved with any microscopy modality, and for the optical wavelengths in common usage the effects of scattering dominate those of light absorption (Lecoq and Schnitzer, 2011). It was these depth limitations due to scattering that prompted the development of microendoscopy as a means of imaging cells in deep brain areas (Jung et al., 2004; Jung and Schnitzer, 2003; Levene et al., 2004). Recent work has demonstrated the gains in imaging depth that are achievable by using longer wavelength infrared illumination, which undergoes markedly reduced scattering in tissue (Kobat et al., 2011). Notably, in vivo three-photon fluorescence microscopy using an excitation wavelength of 1.7 μm can provide images from the dorsal surface of the mouse neocortex down to area CA1 of hippocampus, about ~1.1 mm deep in tissue (Horton et al., 2013) (Figure 5). Much work would be necessary to make this approach viable as a generally applicable platform for imaging neural activity in behaving mice. A combination of red-shifted activity indicators, optical elements optimized for 1.7-μm-wavelength illumination, new light sources emitting ultrashort pulses at this wavelength, and methods of adaptive optics (Ji et al., 2010; Rueckel et al., 2006; Wang et al., 2014) for correcting the optical wavefront aberrations that arise deep in tissue would likely all be required.

To achieve these multiple elements in a form that worked well collectively, multi-disciplinary collaboration will almost certainly be necessary. More generally, this example is but one illustration that the challenges of imaging cellular level activity in behaving mammals are sufficiently great that future progress will benefit

hugely from close cooperation between neuroscientists, protein designers, optical engineers, statisticians, and computer scientists, while adhering to the systems engineering approach. Indicators, optical instrumentation, and computational algorithms are constantly evolving, but the physics of light and the need to detect adequate numbers of photons will always set the physical bounds on optical imaging capabilities. Hence, the systems engineering perspective will invariably provide valuable insights.

REFERENCES

Ahrens, M.B., Orger, M.B., Robson, D.N., Li, J.M., and Keller, P.J. (2013). Whole-brain functional imaging at cellular resolution using light-sheet microscopy. Nat. Methods 10, 413–420.

Akemann, W., Mutoh, H., Perron, A., Rossier, J., and Knöpfel, T. (2010). Imaging brain electric signals with genetically targeted voltage-sensitive fluorescent proteins. Nat. Methods 7, 643–649.

Akemann, W., Mutoh, H., Perron, A., Park, Y.K., Iwamoto, Y., and Knöpfel, T. (2012). Imaging neural circuit dynamics with a voltage-sensitive fluorescent protein. J. Neurophysiol. 108, 2323–2337.

Akerboom, J., Carreras Calderón, N., Tian, L., Wabnig, S., Prigge, M., Tolö, J., Gordus, A., Orger, M.B., Severi, K.E., Macklin, J.J., et al. (2013). Genetically encoded calcium indicators for multi-color neural activity imaging and combination with optogenetics. Front. Mol. Neurosci. 6, 2.

Alivisatos, A.P., Andrews, A.M., Boyden, E.S., Chun, M., Church, G.M., Deisseroth, K., Donoghue, J.P., Fraser, S.E., Lippincott-Schwartz, J., Looger, L.L., et al. (2013). Nanotools for neuroscience and brain activity mapping. ACS Nano 7, 1850–1866.

Andermann, M.L., Kerlin, A.M., and Reid, R.C. (2010). Chronic cellular imaging of mouse visual cortex during operant behavior and passive viewing. Front. Cell. Neurosci. 4, 3.

Andermann, M.L., Kerlin, A.M., Roumis, D.K., Glickfeld, L.L., and Reid, R.C. (2011). Functional specialization of mouse higher visual cortical areas. Neuron 72, 1025–1039.

Andermann, M.L., Gilfoy, N.B., Goldey, G.J., Sachdev, R.N., Wölfel, M., McCormick, D.A., Reid, R.C., and Levene, M.J. (2013). Chronic cellular imaging of entire cortical columns in awake mice using microprisms. Neuron 80, 900–913.

Anselmi, F., Ventalon, C., Bègue, A., Ogden, D., and Emiliani, V. (2011). Three-dimensional imaging and photostimulation by remote-focusing and holographic light patterning. Proc. Natl. Acad. Sci. USA 108, 19504–19509.

Antić, S., and Zecević, D. (1995). Optical signals from neurons with internally applied voltage-sensitive dyes. J. Neurosci. 15, 1392–1405.

Aronov, D., and Tank, D.W. (2014). Engagement of neural circuits underlying 2D spatial navigation in a rodent virtual reality system. Neuron 84, 442–456.

Barretto, R.P., Messerschmidt, B., and Schnitzer, M.J. (2009). In vivo fluorescence imaging with high-resolution microlenses. Nat. Methods 6, 511–512.

Barretto, R.P.J., Ko, T.H., Jung, J.C., Wang, T.J., Capps, G., Waters, A.C., Ziv, Y., Attardo, A., Recht, L., and Schnitzer, M.J. (2011). Time-lapse imaging of

disease progression in deep brain areas using fluorescence microendoscopy. Nat. Med. 17, 223–228.

Bathellier, B., Ushakova, L., and Rumpel, S. (2012). Discrete neocortical dynamics predict behavioral categorization of sounds. Neuron 76, 435–449.

Batista, A.P., Buneo, C.A., Snyder, L.H., and Andersen, R.A. (1999). Reach plans in eye-centered coordinates. Science 285, 257–260.

Bègue, A., Papagiakoumou, E., Leshem, B., Conti, R., Enke, L., Oron, D., and Emiliani, V. (2013). Two-photon excitation in scattering media by spatiotemporally shaped beams and their application in optogenetic stimulation. Biomed. Opt. Express 4, 2869–2879.

Bell, A.J., and Sejnowski, T.J. (1995). An information-maximization approach to blind separation and blind deconvolution. Neural Comput. 7, 1129–1159.

Berdyyeva, T., Otte, S., Aluisio, L., Ziv, Y., Burns, L.D., Dugovic, C., Yun, S., Ghosh, K.K., Schnitzer, M.J., Lovenberg, T., and Bonaventure, P. (2014). Zolpidem reduces hippocampal neuronal activity in freely behaving mice: a large scale calcium imaging study with miniaturized fluorescence microscope. PLoS ONE 9, e112068.

Blauvelt, D.G., Sato, T.F., Wienisch, M., Knöpfel, T., and Murthy, V.N. (2013). Distinct spatiotemporal activity in principal neurons of the mouse olfactory bulb in anesthetized and awake states. Front. Neural Circuits 7, 46.

Bouchard, M.B., Voleti, V., Mendes, C.S., Lacefield, C., Grueber, W.B., Mann, R.S., Bruno, R.M., and Hillman, E.M. (2015). Swept confocally-aligned planar excitation (SCAPE) microscopy for high speed volumetric imaging of behaving organisms. Nat. Photonics 9, 113–119.

Boyd, A.M., Kato, H.K., Komiyama, T., and Isaacson, J.S. (2015). Broadcasting of cortical activity to the olfactory bulb. Cell Rep. 10, 1032–1039.

BRAIN Initiative (2014). BRAIN 2025: A Scientific Vision. (U.S. Department of Health & Human Services (HHS)). http://www.braininitiative.nih.gov/2025/index.htm.

Brown, G.D., Yamada, S., and Sejnowski, T.J. (2001). Independent component analysis at the neural cocktail party. Trends Neurosci. 24, 54–63.

Broxton, M., Grosenick, L., Yang, S., Cohen, N., Andalman, A., Deisseroth, K., and Levoy, M. (2013). Wave optics theory and 3-D deconvolution for the light field microscope. Opt. Express 21, 25418–25439.

Cao, G., Platisa, J., Pieribone, V.A., Raccuglia, D., Kunst, M., and Nitabach, M.N. (2013). Genetically targeted optical electrophysiology in intact neural circuits. Cell 154, 904–913.

Carandini, M., Shimaoka, D., Rossi, L.F., Sato, T.K., Benucci, A., and Knöpfel, T. (2015). Imaging the awake visual cortex with a genetically encoded voltage indicator. J. Neurosci. 35, 53–63.

Carey, R.M., Verhagen, J.V., Wesson, D.W., Pírez, N., and Wachowiak, M. (2009). Temporal structure of receptor neuron input to the olfactory bulb imaged in behaving rats. J. Neurophysiol. 101, 1073–1088.

Chen, J.L., Andermann, M.L., Keck, T., Xu, N.L., and Ziv, Y. (2013a). Imaging neuronal populations in behaving rodents: paradigms for studying neural circuits underlying behavior in the mammalian cortex. J. Neurosci. 33, 17631–17640.

Chen, J.L., Carta, S., Soldado-Magraner, J., Schneider, B.L., and Helmchen, F. (2013b). Behaviour-dependent recruitment of long-range projection neurons in somatosensory cortex. Nature 499, 336–340.

Chen, T.-W., Wardill, T.J., Sun, Y., Pulver, S.R., Renninger, S.L., Baohan, A., Schreiter, E.R., Kerr, R.A., Orger, M.B., Jayaraman, V., et al. (2013c). Ultrasensitive fluorescent proteins for imaging neuronal activity. Nature 499, 295–300.

Chia, T.H., and Levene, M.J. (2009). Microprisms for in vivo multilayer cortical imaging. J. Neurophysiol. 102, 1310–1314.

Chow, B.Y., Han, X., Dobry, A.S., Qian, X., Chuong, A.S., Li, M., Henninger, M.A., Belfort, G.M., Lin, Y., Monahan, P.E., and Boyden, E.S. (2010). High-performance genetically targetable optical neural silencing by light-driven proton pumps. Nature 463, 98–102.

Chung, K., Wallace, J., Kim, S.Y., Kalyanasundaram, S., Andalman, A.S., Davidson, T.J., Mirzabekov, J.J., Zalocusky, K.A., Mattis, J., Denisin, A.K.,

et al. (2013). Structural and molecular interrogation of intact biological systems. Nature *497*, 332–337.

Clancy, K.B., Koralek, A.C., Costa, R.M., Feldman, D.E., and Carmena, J.M. (2014). Volitional modulation of optically recorded calcium signals during neuroprosthetic learning. Nat. Neurosci. *17*, 807–809.

Cyranoski, D. (2014). Marmosets are stars of Japan's ambitious brain project. Nature *514*, 151–152.

Dimitrov, D., He, Y., Mutoh, H., Baker, B.J., Cohen, L., Akemann, W., and Knöpfel, T. (2007). Engineering and characterization of an enhanced fluorescent protein voltage sensor. PLoS ONE *2*, e440.

Dombeck, D.A., Khabbaz, A.N., Collman, F., Adelman, T.L., and Tank, D.W. (2007). Imaging large-scale neural activity with cellular resolution in awake, mobile mice. Neuron *56*, 43–57.

Dombeck, D.A., Graziano, M.S., and Tank, D.W. (2009). Functional clustering of neurons in motor cortex determined by cellular resolution imaging in awake behaving mice. J. Neurosci. *29*, 13751–13760.

Dombeck, D.A., Harvey, C.D., Tian, L., Looger, L.L., and Tank, D.W. (2010). Functional imaging of hippocampal place cells at cellular resolution during virtual navigation. Nat. Neurosci. *13*, 1433–1440.

Duemani Reddy, G., Kelleher, K., Fink, R., and Saggau, P. (2008). Three-dimensional random access multiphoton microscopy for functional imaging of neuronal activity. Nat. Neurosci. *11*, 713–720.

Engelbrecht, C.J., Johnston, R.S., Seibel, E.J., and Helmchen, F. (2008). Ultra-compact fiber-optic two-photon microscope for functional fluorescence imaging in vivo. Opt. Express *16*, 5556–5564.

Ferezou, I., Bolea, S., and Petersen, C.C. (2006). Visualizing the cortical representation of whisker touch: voltage-sensitive dye imaging in freely moving mice. Neuron *50*, 617–629.

Ferezou, I., Haiss, F., Gentet, L.J., Aronoff, R., Weber, B., and Petersen, C.C.H. (2007). Spatiotemporal dynamics of cortical sensorimotor integration in behaving mice. Neuron *56*, 907–923.

Flusberg, B.A., Jung, J.C., Cocker, E.D., Anderson, E.P., and Schnitzer, M.J. (2005). In vivo brain imaging using a portable 3.9 gram two-photon fluorescence microendoscope. Opt. Lett. *30*, 2272–2274.

Flusberg, B.A., Nimmerjahn, A., Cocker, E.D., Mukamel, E.A., Barretto, R.P.J., Ko, T.H., Burns, L.D., Jung, J.C., and Schnitzer, M.J. (2008). High-speed, miniaturized fluorescence microscopy in freely moving mice. Nat. Methods *5*, 935–938.

Flytzanis, N.C., Bedbrook, C.N., Chiu, H., Engqvist, M.K., Xiao, C., Chan, K.Y., Sternberg, P.W., Arnold, F.H., and Gradinaru, V. (2014). Archaerhodopsin variants with enhanced voltage-sensitive fluorescence in mammalian and Caenorhabditis elegans neurons. Nat. Commun. *5*, 4894.

Freeman, J., Vladimirov, N., Kawashima, T., Mu, Y., Sofroniew, N.J., Bennett, D.V., Rosen, J., Yang, C.T., Looger, L.L., and Ahrens, M.B. (2014). Mapping brain activity at scale with cluster computing. Nat. Methods *11*, 941–950.

Funahashi, S., Bruce, C.J., and Goldman-Rakic, P.S. (1989). Mnemonic coding of visual space in the monkey's dorsolateral prefrontal cortex. J. Neurophysiol. *61*, 331–349.

Fuster, J.M., and Alexander, G.E. (1971). Neuron activity related to short-term memory. Science *173*, 652–654.

Ghosh, K.K., Burns, L.D., Cocker, E.D., Nimmerjahn, A., Ziv, Y., Gamal, A.E., and Schnitzer, M.J. (2011). Miniaturized integration of a fluorescence microscope. Nat. Methods *8*, 871–878.

Glickfeld, L.L., Andermann, M.L., Bonin, V., and Reid, R.C. (2013). Cortico-cortical projections in mouse visual cortex are functionally target specific. Nat. Neurosci. *16*, 219–226.

Göbel, W., Kerr, J.N.D., Nimmerjahn, A., and Helmchen, F. (2004). Miniaturized two-photon microscope based on a flexible coherent fiber bundle and a gradient-index lens objective. Opt. Lett. *29*, 2521–2523.

Göbel, W., Kampa, B.M., and Helmchen, F. (2007). Imaging cellular network dynamics in three dimensions using fast 3D laser scanning. Nat. Methods *4*, 73–79.

Gong, Y., Li, J.Z., and Schnitzer, M.J. (2013). Enhanced Archaerhodopsin Fluorescent Protein Voltage Indicators. PLoS ONE *8*, e66959.

Gong, Y., Wagner, M.J., Zhong Li, J., and Schnitzer, M.J. (2014). Imaging neural spiking in brain tissue using FRET-opsin protein voltage sensors. Nat. Commun. *5*, 3674.

Greenberg, D.S., and Kerr, J.N. (2009). Automated correction of fast motion artifacts for two-photon imaging of awake animals. J. Neurosci. Methods *176*, 1–15.

Greenberg, D.S., Houweling, A.R., and Kerr, J.N.D. (2008). Population imaging of ongoing neuronal activity in the visual cortex of awake rats. Nat. Neurosci. *11*, 749–751.

Grewe, B.F., Langer, D., Kasper, H., Kampa, B.M., and Helmchen, F. (2010). High-speed in vivo calcium imaging reveals neuronal network activity with near-millisecond precision. Nat. Methods *7*, 399–405.

Grinvald, A., Frostig, R.D., Siegel, R.M., and Bartfeld, E. (1991). High-resolution optical imaging of functional brain architecture in the awake monkey. Proc. Natl. Acad. Sci. USA *88*, 11559–11563.

Hafting, T., Fyhn, M., Molden, S., Moser, M.B., and Moser, E.I. (2005). Microstructure of a spatial map in the entorhinal cortex. Nature *436*, 801–806.

Hama, H., Kurokawa, H., Kawano, H., Ando, R., Shimogori, T., Noda, H., Fukami, K., Sakaue-Sawano, A., and Miyawaki, A. (2011). Scale: a chemical approach for fluorescence imaging and reconstruction of transparent mouse brain. Nat. Neurosci. *14*, 1481–1488.

Harvey, C.D., Collman, F., Dombeck, D.A., and Tank, D.W. (2009). Intracellular dynamics of hippocampal place cells during virtual navigation. Nature *461*, 941–946.

Harvey, C.D., Coen, P., and Tank, D.W. (2012). Choice-specific sequences in parietal cortex during a virtual-navigation decision task. Nature *484*, 62–68.

Helmchen, F., Imoto, K., and Sakmann, B. (1996). Ca2+ buffering and action potential-evoked Ca2+ signaling in dendrites of pyramidal neurons. Biophys. J. *70*, 1069–1081.

Helmchen, F., Svoboda, K., Denk, W., and Tank, D.W. (1999). In vivo dendritic calcium dynamics in deep-layer cortical pyramidal neurons. Nat. Neurosci. *2*, 989–996.

Helmchen, F., Fee, M.S., Tank, D.W., and Denk, W. (2001). A miniature head-mounted two-photon microscope. high-resolution brain imaging in freely moving animals. Neuron *31*, 903–912.

Helmchen, F., Denk, W., and Kerr, J.N. (2013). Miniaturization of two-photon microscopy for imaging in freely moving animals. Cold Spring Harb. Protoc. *2013*, 904–913.

Hendel, T., Mank, M., Schnell, B., Griesbeck, O., Borst, A., and Reiff, D.F. (2008). Fluorescence changes of genetic calcium indicators and OGB-1 correlated with neural activity and calcium in vivo and in vitro. J. Neurosci. *28*, 7399–7411.

Heys, J.G., Rangarajan, K.V., and Dombeck, D.A. (2014). The functional micro-organization of grid cells revealed by cellular-resolution imaging. Neuron *84*, 1079–1090.

Hires, S.A., Tian, L., and Looger, L.L. (2008). Reporting neural activity with genetically encoded calcium indicators. Brain Cell Biol. *36*, 69–86.

Hochbaum, D.R., Zhao, Y., Farhi, S.L., Klapoetke, N., Werley, C.A., Kapoor, V., Zou, P., Kralj, J.M., Maclaurin, D., Smedemark-Margulies, N., et al. (2014). All-optical electrophysiology in mammalian neurons using engineered microbial rhodopsins. Nat. Methods *11*, 825–833.

Holekamp, T.F., Turaga, D., and Holy, T.E. (2008). Fast three-dimensional fluorescence imaging of activity in neural populations by objective-coupled planar illumination microscopy. Neuron *57*, 661–672.

Hölscher, C., Schnee, A., Dahmen, H., Setia, L., and Mallot, H.A. (2005). Rats are able to navigate in virtual environments. J. Exp. Biol. *208*, 561–569.

Horton, N.G., Wang, K., Kobat, D., Clark, C.G., Wise, F.W., Schaffer, C.B., and Xu, C. (2013). In vivo three-photon microscopy of subcortical structures within an intact mouse brain. Nat. Photonics *7*, http://dx.doi.org/10.1038/nphoton.2012.336.

Huber, D., Gutnisky, D.A., Peron, S., O'Connor, D.H., Wiegert, J.S., Tian, L., Oertner, T.G., Looger, L.L., and Svoboda, K. (2012). Multiple dynamic representations in the motor cortex during sensorimotor learning. Nature *484*, 473–478.

Hyvärinen, A., and Oja, E. (2000). Independent component analysis: algorithms and applications. Neural Netw. *13*, 411–430.

Inoue, M., Takeuchi, A., Horigane, S., Ohkura, M., Gengyo-Ando, K., Fujii, H., Kamijo, S., Takemoto-Kimura, S., Kano, M., Nakai, J., et al. (2015). Rational design of a high-affinity, fast, red calcium indicator R-CaMP2. Nat. Methods *12*, 64–70.

Jennings, J.H., Ung, R.L., Resendez, S.L., Stamatakis, A.M., Taylor, J.G., Huang, J., Veleta, K., Kantak, P.A., Aita, M., Shilling-Scrivo, K., et al. (2015). Visualizing hypothalamic network dynamics for appetitive and consummatory behaviors. Cell *160*, 516–527.

Ji, N., Milkie, D.E., and Betzig, E. (2010). Adaptive optics via pupil segmentation for high-resolution imaging in biological tissues. Nat. Methods *7*, 141–147.

Jin, L., Han, Z., Platisa, J., Wooltorton, J.R., Cohen, L.B., and Pieribone, V.A. (2012). Single action potentials and subthreshold electrical events imaged in neurons with a fluorescent protein voltage probe. Neuron *75*, 779–785.

Jung, J.C., and Schnitzer, M.J. (2003). Multiphoton endoscopy. Opt. Lett. *28*, 902–904.

Jung, J.C., Mehta, A.D., Aksay, E., Stepnoski, R., and Schnitzer, M.J. (2004). In vivo mammalian brain imaging using one- and two-photon fluorescence microendoscopy. J. Neurophysiol. *92*, 3121–3133.

Kaifosh, P., Lovett-Barron, M., Turi, G.F., Reardon, T.R., and Losonczy, A. (2013). Septo-hippocampal GABAergic signaling across multiple modalities in awake mice. Nat. Neurosci. *16*, 1182–1184.

Kato, H.K., Chu, M.W., Isaacson, J.S., and Komiyama, T. (2012). Dynamic sensory representations in the olfactory bulb: modulation by wakefulness and experience. Neuron *76*, 962–975.

Katona, G., Szalay, G., Maák, P., Kaszás, A., Veress, M., Hillier, D., Chiovini, B., Vizi, E.S., Roska, B., and Rózsa, B. (2012). Fast two-photon in vivo imaging with three-dimensional random-access scanning in large tissue volumes. Nat. Methods *9*, 201–208.

Keck, T., Keller, G.B., Jacobsen, R.I., Eysel, U.T., Bonhoeffer, T., and Hübener, M. (2013). Synaptic scaling and homeostatic plasticity in the mouse visual cortex in vivo. Neuron *80*, 327–334.

Keller, G.B., Bonhoeffer, T., and Hübener, M. (2012). Sensorimotor mismatch signals in primary visual cortex of the behaving mouse. Neuron *74*, 809–815.

Kerlin, A.M., Andermann, M.L., Berezovskii, V.K., and Reid, R.C. (2010). Broadly tuned response properties of diverse inhibitory neuron subtypes in mouse visual cortex. Neuron *67*, 858–871.

Kerr, J.N.D., Greenberg, D., and Helmchen, F. (2005). Imaging input and output of neocortical networks in vivo. Proc. Natl. Acad. Sci. USA *102*, 14063–14068.

Kitamura, K., Judkewitz, B., Kano, M., Denk, W., and Häusser, M. (2008). Targeted patch-clamp recordings and single-cell electroporation of unlabeled neurons in vivo. Nat. Methods *5*, 61–67.

Kobat, D., Horton, N.G., and Xu, C. (2011). In vivo two-photon microscopy to 1.6-mm depth in mouse cortex. J. Biomed. Opt. *16*, 106014.

Komiyama, T., Sato, T.R., O'Connor, D.H., Zhang, Y.-X., Huber, D., Hooks, B.M., Gabitto, M., and Svoboda, K. (2010). Learning-related fine-scale specificity imaged in motor cortex circuits of behaving mice. Nature *464*, 1182–1186.

Kralj, J.M., Hochbaum, D.R., Douglass, A.D., and Cohen, A.E. (2011). Electrical spiking in Escherichia coli probed with a fluorescent voltage-indicating protein. Science *333*, 345–348.

Kralj, J.M., Douglass, A.D., Hochbaum, D.R., Maclaurin, D., and Cohen, A.E. (2012). Optical recording of action potentials in mammalian neurons using a microbial rhodopsin. Nat. Methods *9*, 90–95.

Kuchibhotla, K.V., Wegmann, S., Kopeikina, K.J., Hawkes, J., Rudinskiy, N., Andermann, M.L., Spires-Jones, T.L., Bacskai, B.J., and Hyman, B.T. (2014). Neurofibrillary tangle-bearing neurons are functionally integrated in cortical circuits in vivo. Proc. Natl. Acad. Sci. USA *111*, 510–514.

Kuhn, B., Denk, W., and Bruno, R.M. (2008). In vivo two-photon voltage-sensitive dye imaging reveals top-down control of cortical layers 1 and 2 during wakefulness. Proc. Natl. Acad. Sci. USA *105*, 7588–7593.

Lanyi, J.K. (2004). Bacteriorhodopsin. Annu. Rev. Physiol. *66*, 665–688.

Lecoq, J., and Schnitzer, M.J. (2011). An infrared fluorescent protein for deeper imaging. Nat. Biotechnol. *29*, 715–716.

Lecoq, J., Savall, J., Vučinić, D., Grewe, B.F., Kim, H., Li, J.Z., Kitch, L.J., and Schnitzer, M.J. (2014). Visualizing mammalian brain area interactions by dual-axis two-photon calcium imaging. Nat. Neurosci. *17*, 1825–1829.

Levene, M.J., Dombeck, D.A., Kasischke, K.A., Molloy, R.P., and Webb, W.W. (2004). In vivo multiphoton microscopy of deep brain tissue. J. Neurophysiol. *91*, 1908–1912.

Levoy, M., Zhang, Z., and McDowall, I. (2009). Recording and controlling the 4D light field in a microscope using microlens arrays. J. Microsc. *235*, 144–162.

Lovett-Barron, M., Kaifosh, P., Kheirbek, M.A., Danielson, N., Zaremba, J.D., Reardon, T.R., Turi, G.F., Hen, R., Zemelman, B.V., and Losonczy, A. (2014). Dendritic inhibition in the hippocampus supports fear learning. Science *343*, 857–863.

Low, R.J., Gu, Y., and Tank, D.W. (2014). Cellular resolution optical access to brain regions in fissures: imaging medial prefrontal cortex and grid cells in entorhinal cortex. Proc. Natl. Acad. Sci. USA *111*, 18739–18744.

Marshall, J.D., and Schnitzer, M.J. (2013). Optical strategies for sensing neuronal voltage using quantum dots and other semiconductor nanocrystals. ACS Nano *7*, 4601–4609.

Maruyama, R., Maeda, K., Moroda, H., Kato, I., Inoue, M., Miyakawa, H., and Aonishi, T. (2014). Detecting cells using non-negative matrix factorization on calcium imaging data. Neural Netw. *55*, 11–19.

Marvin, J.S., Borghuis, B.G., Tian, L., Cichon, J., Harnett, M.T., Akerboom, J., Gordus, A., Renninger, S.L., Chen, T.W., Bargmann, C.I., et al. (2013). An optimized fluorescent probe for visualizing glutamate neurotransmission. Nat. Methods *10*, 162–170.

Masamizu, Y., Tanaka, Y.R., Tanaka, Y.H., Hira, R., Ohkubo, F., Kitamura, K., Isomura, Y., Okada, T., and Matsuzaki, M. (2014). Two distinct layer-specific dynamics of cortical ensembles during learning of a motor task. Nat. Neurosci. *17*, 987–994.

McIsaac, R.S., Engqvist, M.K., Wannier, T., Rosenthal, A.Z., Herwig, L., Flytzanis, N.C., Imasheva, E.S., Lanyi, J.K., Balashov, S.P., Gradinaru, V., and Arnold, F.H. (2014). Directed evolution of a far-red fluorescent rhodopsin. Proc. Natl. Acad. Sci. USA *111*, 13034–13039.

McKeown, M.J., Makeig, S., Brown, G.G., Jung, T.P., Kindermann, S.S., Bell, A.J., and Sejnowski, T.J. (1998). Analysis of fMRI data by blind separation into independent spatial components. Hum. Brain Mapp. *6*, 160–188.

Miller, J.E., Ayzenshtat, I., Carrillo-Reid, L., and Yuste, R. (2014). Visual stimuli recruit intrinsically generated cortical ensembles. Proc. Natl. Acad. Sci. USA *111*, E4053–E4061.

Miri, A., Daie, K., Burdine, R.D., Aksay, E., and Tank, D.W. (2011). Regression-based identification of behavior-encoding neurons during large-scale optical imaging of neural activity at cellular resolution. J. Neurophysiol. *105*, 964–980.

Mohajerani, M.H., McVea, D.A., Fingas, M., and Murphy, T.H. (2010). Mirrored bilateral slow-wave cortical activity within local circuits revealed by fast bihemispheric voltage-sensitive dye imaging in anesthetized and awake mice. J. Neurosci. *30*, 3745–3751.

Mohajerani, M.H., Chan, A.W., Mohsenvand, M., LeDue, J., Liu, R., McVea, D.A., Boyd, J.D., Wang, Y.T., Reimers, M., and Murphy, T.H. (2013). Spontaneous cortical activity alternates between motifs defined by regional axonal projections. Nat. Neurosci. *16*, 1426–1435.

Mukamel, E.A., Nimmerjahn, A., and Schnitzer, M.J. (2009). Automated analysis of cellular signals from large-scale calcium imaging data. Neuron *63*, 747–760.

Muller, A., Joseph, V., Slesinger, P.A., and Kleinfeld, D. (2014). Cell-based reporters reveal in vivo dynamics of dopamine and norepinephrine release in murine cortex. Nat. Methods *11*, 1245–1252.

Murayama, M., and Larkum, M.E. (2009). Enhanced dendritic activity in awake rats. Proc. Natl. Acad. Sci. USA *106*, 20482–20486.

Murayama, M., Pérez-Garci, E., Lüscher, H.-R., and Larkum, M.E. (2007). Fiberoptic system for recording dendritic calcium signals in layer 5 neocortical pyramidal cells in freely moving rats. J. Neurophysiol. *98*, 1791–1805.

Murayama, M., Pérez-Garci, E., Nevian, T., Bock, T., Senn, W., and Larkum, M.E. (2009). Dendritic encoding of sensory stimuli controlled by deep cortical interneurons. Nature *457*, 1137–1141.

Nakai, J., Ohkura, M., and Imoto, K. (2001). A high signal-to-noise Ca(2+) probe composed of a single green fluorescent protein. Nat. Biotechnol. *19*, 137–141.

Newsome, W.T., Britten, K.H., and Movshon, J.A. (1989). Neuronal correlates of a perceptual decision. Nature *341*, 52–54.

Nikolenko, V., Peterka, D.S., Araya, R., Woodruff, A., and Yuste, R. (2013). Spatial light modulator microscopy. Cold Spring Harb. Protoc. *2013*, 1132–1141.

Nimmerjahn, A., Kirchhoff, F., Kerr, J.N., and Helmchen, F. (2004). Sulforhodamine 101 as a specific marker of astroglia in the neocortex in vivo. Nat. Methods *1*, 31–37.

Nimmerjahn, A., Mukamel, E.A., and Schnitzer, M.J. (2009). Motor behavior activates Bergmann glial networks. Neuron *62*, 400–412.

O'Connor, D.H., Peron, S.P., Huber, D., and Svoboda, K. (2010). Neural activity in barrel cortex underlying vibrissa-based object localization in mice. Neuron *67*, 1048–1061.

O'Keefe, J., and Dostrovsky, J. (1971). The hippocampus as a spatial map. Preliminary evidence from unit activity in the freely-moving rat. Brain Res. *34*, 171–175.

Ohki, K., Chung, S., Ch'ng, Y.H., Kara, P., and Reid, R.C. (2005). Functional imaging with cellular resolution reveals precise micro-architecture in visual cortex. Nature *433*, 597–603.

Ohkura, M., Sasaki, T., Sadakari, J., Gengyo-Ando, K., Kagawa-Nagamura, Y., Kobayashi, C., Ikegaya, Y., and Nakai, J. (2012). Genetically encoded green fluorescent Ca2+ indicators with improved detectability for neuronal Ca2+ signals. PLoS ONE *7*, e51286.

Ozden, I., Lee, H.M., Sullivan, M.R., and Wang, S.S.-H. (2008). Identification and clustering of event patterns from in vivo multiphoton optical recordings of neuronal ensembles. J. Neurophysiol. *100*, 495–503.

Packer, A.M., Peterka, D.S., Hirtz, J.J., Prakash, R., Deisseroth, K., and Yuste, R. (2012). Two-photon optogenetics of dendritic spines and neural circuits. Nat. Methods *9*, 1202–1205.

Packer, A.M., Russell, L.E., Dalgleish, H.W., and Häusser, M. (2015). Simultaneous all-optical manipulation and recording of neural circuit activity with cellular resolution in vivo. Nat. Methods *12*, 140–146.

Patterson, M.A., Lagier, S., and Carleton, A. (2013). Odor representations in the olfactory bulb evolve after the first breath and persist as an odor afterimage. Proc. Natl. Acad. Sci. USA *110*, E3340–E3349.

Peterka, D.S., Takahashi, H., and Yuste, R. (2011). Imaging voltage in neurons. Neuron *69*, 9–21.

Peters, A.J., Chen, S.X., and Komiyama, T. (2014). Emergence of reproducible spatiotemporal activity during motor learning. Nature *510*, 263–267.

Petreanu, L., Gutnisky, D.A., Huber, D., Xu, N.L., O'Connor, D.H., Tian, L., Looger, L., and Svoboda, K. (2012). Activity in motor-sensory projections reveals distributed coding in somatosensation. Nature *489*, 299–303.

Pfeiffer, B.E., and Foster, D.J. (2013). Hippocampal place-cell sequences depict future paths to remembered goals. Nature *497*, 74–79.

Piyawattanametha, W., Cocker, E.D., Burns, L.D., Barretto, R.P., Jung, J.C., Ra, H., Solgaard, O., and Schnitzer, M.J. (2009). In vivo brain imaging using a portable 2.9 g two-photon microscope based on a microelectromechanical systems scanning mirror. Opt. Lett. *34*, 2309–2311.

Prakash, R., Yizhar, O., Grewe, B., Ramakrishnan, C., Wang, N., Goshen, I., Packer, A.M., Peterka, D.S., Yuste, R., Schnitzer, M.J., and Deisseroth, K. (2012). Two-photon optogenetic toolbox for fast inhibition, excitation and bistable modulation. Nat. Methods *9*, 1171–1179.

Prevedel, R., Yoon, Y.G., Hoffmann, M., Pak, N., Wetzstein, G., Kato, S., Schrödel, T., Raskar, R., Zimmer, M., Boyden, E.S., and Vaziri, A. (2014). Simultaneous whole-animal 3D imaging of neuronal activity using light-field microscopy. Nat. Methods *11*, 727–730.

Quirin, S., Jackson, J., Peterka, D.S., and Yuste, R. (2014). Simultaneous imaging of neural activity in three dimensions. Front. Neural Circuits *8*, 29.

Raffi, M., and Siegel, R.M. (2005). Functional architecture of spatial attention in the parietal cortex of the behaving monkey. J. Neurosci. *25*, 5171–5186.

Ravassard, P., Kees, A., Willers, B., Ho, D., Aharoni, D., Cushman, J., Aghajan, Z.M., and Mehta, M.R. (2013). Multisensory control of hippocampal spatiotemporal selectivity. Science *340*, 1342–1346.

Reidl, J., Starke, J., Omer, D.B., Grinvald, A., and Spors, H. (2007). Independent component analysis of high-resolution imaging data identifies distinct functional domains. Neuroimage *34*, 94–108.

Reutsky-Gefen, I., Golan, L., Farah, N., Schejter, A., Tsur, L., Brosh, I., and Shoham, S. (2013). Holographic optogenetic stimulation of patterned neuronal activity for vision restoration. Nat. Commun. *4*, 1509.

Rickgauer, J.P., Deisseroth, K., and Tank, D.W. (2014). Simultaneous cellular-resolution optical perturbation and imaging of place cell firing fields. Nat. Neurosci. *17*, 1816–1824.

Rueckel, M., Mack-Bucher, J.A., and Denk, W. (2006). Adaptive wavefront correction in two-photon microscopy using coherence-gated wavefront sensing. Proc. Natl. Acad. Sci. USA *103*, 17137–17142.

Runyan, C.A., Schummers, J., Van Wart, A., Kuhlman, S.J., Wilson, N.R., Huang, Z.J., and Sur, M. (2010). Response features of parvalbumin-expressing interneurons suggest precise roles for subtypes of inhibition in visual cortex. Neuron *67*, 847–857.

Sasaki, T., Takahashi, N., Matsuki, N., and Ikegaya, Y. (2008). Fast and accurate detection of action potentials from somatic calcium fluctuations. J. Neurophysiol. *100*, 1668–1676.

Sawinski, J., Wallace, D.J., Greenberg, D.S., Grossmann, S., Denk, W., and Kerr, J.N.D. (2009). Visually evoked activity in cortical cells imaged in freely moving animals. Proc. Natl. Acad. Sci. USA *106*, 19557–19562.

Scott, B.B., Brody, C.D., and Tank, D.W. (2013). Cellular resolution functional imaging in behaving rats using voluntary head restraint. Neuron *80*, 371–384.

Seidemann, E., Arieli, A., Grinvald, A., and Slovin, H. (2002). Dynamics of depolarization and hyperpolarization in the frontal cortex and saccade goal. Science *295*, 862–865.

Sheffield, M.E., and Dombeck, D.A. (2015). Calcium transient prevalence across the dendritic arbour predicts place field properties. Nature *517*, 200–204.

Sjulson, L., and Miesenböck, G. (2007). Optical recording of action potentials and other discrete physiological events: a perspective from signal detection theory. Physiology (Bethesda) *22*, 47–55.

Soden, M.E., Jones, G.L., Sanford, C.A., Chung, A.S., Güler, A.D., Chavkin, C., Luján, R., and Zweifel, L.S. (2013). Disruption of dopamine neuron activity pattern regulation through selective expression of a human KCNN3 mutation. Neuron *80*, 997–1009.

Sofroniew, N.J., Cohen, J.D., Lee, A.K., and Svoboda, K. (2014). Natural whisker-guided behavior by head-fixed mice in tactile virtual reality. J. Neurosci. *34*, 9537–9550.

St-Pierre, F., Marshall, J.D., Yang, Y., Gong, Y., Schnitzer, M.J., and Lin, M.Z. (2014). High-fidelity optical reporting of neuronal electrical activity with an ultrafast fluorescent voltage sensor. Nat. Neurosci. *17*, 884–889.

Stirman, J.N., Smith, I.T., Kudenov, M.W., and Smith, S.L. (2014). Wide field-of-view, twin-region two-photon imaging across extended cortical networks. bioRxiv. http://dx.doi.org/10.1101/011320.

Stosiek, C., Garaschuk, O., Holthoff, K., and Konnerth, A. (2003). In vivo two-photon calcium imaging of neuronal networks. Proc. Natl. Acad. Sci. USA *100*, 7319–7324.

Sun, X.R., Badura, A., Pacheco, D.A., Lynch, L.A., Schneider, E.R., Taylor, M.P., Hogue, I.B., Enquist, L.W., Murthy, M., and Wang, S.S. (2013). Fast GCaMPs for improved tracking of neuronal activity. Nat. Commun. *4*, 2170.

Susaki, E.A., Tainaka, K., Perrin, D., Kishino, F., Tawara, T., Watanabe, T.M., Yokoyama, C., Onoe, H., Eguchi, M., Yamaguchi, S., et al. (2014). Whole-brain imaging with single-cell resolution using chemical cocktails and computational analysis. Cell *157*, 726–739.

Svoboda, K., Helmchen, F., Denk, W., and Tank, D.W. (1999). Spread of dendritic excitation in layer 2/3 pyramidal neurons in rat barrel cortex in vivo. Nat. Neurosci. *2*, 65–73.

Tanigawa, H., Lu, H.D., and Roe, A.W. (2010). Functional organization for color and orientation in macaque V4. Nat. Neurosci. *13*, 1542–1548.

Thévenaz, P., Ruttimann, U.E., and Unser, M. (1998). A pyramid approach to subpixel registration based on intensity. IEEE Trans. Image Process. *7*, 27–41.

Tian, L., Hires, S.A., Mao, T., Huber, D., Chiappe, M.E., Chalasani, S.H., Petreanu, L., Akerboom, J., McKinney, S.A., Schreiter, E.R., et al. (2009). Imaging neural activity in worms, flies and mice with improved GCaMP calcium indicators. Nat. Methods *6*, 875–881.

Tian, L., Yang, Y., Wysocki, L.M., Arnold, A.C., Hu, A., Ravichandran, B., Sternson, S.M., Looger, L.L., and Lavis, L.D. (2012). Selective esterase-ester pair for targeting small molecules with cellular specificity. Proc. Natl. Acad. Sci. USA *109*, 4756–4761.

Tomer, R., Ye, L., Hsueh, B., and Deisseroth, K. (2014). Advanced CLARITY for rapid and high-resolution imaging of intact tissues. Nat. Protoc. *9*, 1682–1697.

Tsutsui, H., Karasawa, S., Okamura, Y., and Miyawaki, A. (2008). Improving membrane voltage measurements using FRET with new fluorescent proteins. Nat. Methods *5*, 683–685.

Verhagen, J.V., Wesson, D.W., Netoff, T.I., White, J.A., and Wachowiak, M. (2007). Sniffing controls an adaptive filter of sensory input to the olfactory bulb. Nat. Neurosci. *10*, 631–639.

Vogelstein, J.T., Packer, A.M., Machado, T.A., Sippy, T., Babadi, B., Yuste, R., and Paninski, L. (2010). Fast nonnegative deconvolution for spike train inference from population calcium imaging. J. Neurophysiol. *104*, 3691–3704.

Wang, C., Liu, R., Milkie, D.E., Sun, W., Tan, Z., Kerlin, A., Chen, T.W., Kim, D.S., and Ji, N. (2014). Multiplexed aberration measurement for deep tissue imaging in vivo. Nat. Methods *11*, 1037–1040.

Watson, B.O., Nikolenko, V., Araya, R., Peterka, D.S., Woodruff, A., and Yuste, R. (2010). Two-photon microscopy with diffractive optical elements and spatial light modulators. Front. Neurosci. *4*, 29.

Wilt, B.A., Burns, L.D., Wei Ho, E.T., Ghosh, K.K., Mukamel, E.A., and Schnitzer, M.J. (2009). Advances in light microscopy for neuroscience. Annu. Rev. Neurosci. *32*, 435–506.

Wilt, B.A., Fitzgerald, J.E., and Schnitzer, M.J. (2013). Photon shot noise limits on optical detection of neuronal spikes and estimation of spike timing. Biophys. J. *104*, 51–62.

Wu, J., Liu, L., Matsuda, T., Zhao, Y., Rebane, A., Drobizhev, M., Chang, Y.F., Araki, S., Arai, Y., March, K., et al. (2013). Improved orange and red $Ca^2\pm$ indicators and photophysical considerations for optogenetic applications. ACS Chem. Neurosci. *4*, 963–972.

Xu, N.L., Harnett, M.T., Williams, S.R., Huber, D., O'Connor, D.H., Svoboda, K., and Magee, J.C. (2012). Nonlinear dendritic integration of sensory and motor input during an active sensing task. Nature *492*, 247–251.

Yaksi, E., and Friedrich, R.W. (2006). Reconstruction of firing rate changes across neuronal populations by temporally deconvolved Ca2+ imaging. Nat. Methods *3*, 377–383.

Yang, B., Treweek, J.B., Kulkarni, R.P., Deverman, B.E., Chen, C.K., Lubeck, E., Shah, S., Cai, L., and Gradinaru, V. (2014). Single-cell phenotyping within transparent intact tissue through whole-body clearing. Cell *158*, 945–958.

Zhang, Q.F., Wen, Y., Zhang, D., She, L., Wu, J.Y., Dan, Y., and Poo, M.M. (2012). Priming with real motion biases visual cortical response to bistable apparent motion. Proc. Natl. Acad. Sci. USA *109*, 20691–20696.

Zhao, Y., Araki, S., Wu, J., Teramoto, T., Chang, Y.F., Nakano, M., Abdelfattah, A.S., Fujiwara, M., Ishihara, T., Nagai, T., and Campbell, R.E. (2011). An expanded palette of genetically encoded Ca^{2+} indicators. Science *333*, 1888–1891.

Ziv, Y., Burns, L.D., Cocker, E.D., Hamel, E.O., Ghosh, K.K., Kitch, L.J., El Gamal, A., and Schnitzer, M.J. (2013). Long-term dynamics of CA1 hippocampal place codes. Nat. Neurosci. *16*, 264–266.

Zou, P., Zhao, Y., Douglass, A.D., Hochbaum, D.R., Brinks, D., Werley, C.A., Harrison, D.J., Campbell, R.E., and Cohen, A.E. (2014). Bright and fast multicoloured voltage reporters via electrochromic FRET. Nat. Commun. *5*, 4625.